

Tidal Heating of the Lunar Magma Ocean

Wenhao Zhao^{1*}, Harriet Lau¹, Stephen Parman¹, James W. Head III¹

¹Department of Earth, Environmental and Planetary Sciences, Brown University, Providence, RI 02912, USA

*Corresponding author. Email: wenhao_zhao@brown.edu

Abstract

The timing of the lunar magma ocean (LMO) solidification is governed by its thermal evolution. A key geochronological observation is that all analyzed products of LMO solidification have ages (or age peaks) near 4.35 ± 0.05 billion years ago (Ga), suggesting rapid solidification of the last $\sim 40\%$ of the LMO at that time. The ages raise two questions: (1) how was the final solidification of the LMO delayed for over 100 Myr (million years) from the Moon's formation, and (2) after such a delay, how did it solidify so quickly? These two aspects of the ages are inconsistent with models of early-fast solidification or slow-prolonged solidification, controlled by radiogenic heat production and convective cooling (even if slowed by a conductive lithosphere). We propose that both aspects can not only be explained by tidal heating of the LMO but are in fact robust and expected thermal evolution features of a magma ocean cooling while being tidally heated and, in the Moon's case, receding from the Earth. The delay in solidification is due to the LMO being trapped at a stable equilibrium between the enhanced tidal heating rate and the decreasing cooling rate. The rapid solidification at ~ 4.35 Ga occurs when the Moon retreats to the point where an unstable equilibrium is reached, where tidal heating is drastically reduced, rapidly cooling the Moon. Moreover, an unanticipated outcome of our modeling is that the farside of the Moon is predicted to be $20\text{--}60$ °C cooler than the nearside for $\sim 10\text{--}100$ Myr during the final solidification stage. This is consistent with previous studies indicating asymmetric crystallization of the LMO from the farside to the nearside, which leads to an older and less evolved farside crust than the nearside, consistent with the observed higher Mg# of farside anorthositic crust and concentration of H₂O, KREEP, and high Fe-Ti components on the nearside.

The Moon is thought to have started from a fully molten state after a Mars-sized body impacted the proto-Earth, producing a global lunar magma ocean (LMO) [16, 17, 56]. Due to its small size, simple convective cooling would have caused the LMO to cool and completely solidify very rapidly ($< 10^6$ years) [17, 46]. However, all dated products of LMO solidification—mare basaltic sources (pyroxene-bearing), ferroan anorthosites (FANs), and urKREEP (KREEP = K [potassium], REE [rare earth elements], P [phosphorus])—along with detrital zircons and products of cumulate overturn (Mg-suite), have ages, or age peaks, within a surprisingly young and narrow range of 4.35 ± 0.05 Ga [8–10] (Fig. 1A). While the narrow age range is compatible with rapid cooling, the late age (over 100 Myr after Moon formation) is not explained by convective cooling models [6].

Several studies have advocated slow cooling to explain the young ages of LMO crystallization products. Mechanisms include crustal insulation and transient atmospheric blanketing [17, 33], but

these struggle to extend LMO solidification by more than ~ 100 Myr. Moreover, such a prolonged cooling would produce a range of crystallization ages in LMO products, from ~ 4.50 to 4.35 Ga (Fig. 1B), not the observed cluster near 4.35 Ga. A different class of models explains the ages by invoking a single post-solidification reheating episode (Fig. 1C). In this view, the LMO solidifies early, and a later event—e.g., the South Pole–Aitken (SPA) basin–forming impact or Laplace Plane Transition (LPT) tidal heating—resets radiometric ages within the lithosphere to 4.35 Ga [26, 39]. However, these reheating scenarios implicitly require that the SPA impact or LPT event occur at ~ 4.35 Ga, a timing that appears difficult to reconcile with current data and theory [13, 18, 39, 51]. Even if the dates aligned, such events would need to (i) fully reset the ages of all LMO products while (ii) preserving major surface morphologies (e.g., large impact basins and the fossil tidal bulge) and (iii) remain weak enough to avoid initiating ~ 4.35 Ga mare volcanism. In short, prevailing models of LMO thermal evolution do not produce the delayed and then rapid solidification of the LMO at ~ 4.35 Ga.

We propose that both aspects of LMO geochronology can be explained if the thermal evolution of the LMO was controlled by tidal heating raised by the Earth. Tidal heating is the conversion of orbital and rotational energy into internal heat under periodic deformation [27, 48]. Lunar tidal heating has been examined in multiple papers [27, 28, 43]. However, to our knowledge, dissipation within the LMO itself has not been explored in depth. The tidal heating rate is controlled primarily by (1) the strength of Earth’s gravitational forcing and (2) the Moon’s tidal response. Because the Earth–Moon separation during the LMO interval was much smaller than today, Earth’s forcing was correspondingly stronger, as the tidal heating rate is inversely proportional to the sixth power of the distance [18, 48]. Yet, even at smaller separation distances, a rigid, elastic Moon would dissipate little energy, as its deformational response would be weak. Most prior studies adopted a nearly elastic, rigid interior as a starting point, and so concluded that tidal heating was minimal [27, 28, 43]. However, tidal heating rates in a partially molten Moon are greatly enhanced.

As melt solidifies, its viscosity changes from low, fluid-like values, which exhibit low dissipation due to low tidal friction, to high, solid-like values, which similarly exhibit low tidal dissipation due to mostly elastic deformation. Between these low-tidal-dissipative regimes, dissipation in the transitional rheology regime is greatly enhanced (Fig. 2, red curves) and can exceed that in either a pure melt or a pure solid by several orders of magnitude [7, 24, 35]. The heating rate peaks when the Earth’s tidal forcing frequency matches the Moon’s viscoelastic relaxation rate, which corresponds to a transitional rheology [21]; see Supplementary Text. This typically occurs between 50 and 70% solidification [1, 5, 16, 50]. Due to this effect, as the magma ocean cools and crystallizes, tidal heating rises rapidly by multiple orders of magnitude, until it equals the heat-loss rate from the surface (Fig. 2). This point is a stable equilibrium where any perturbation by cooling (or heating) will result in a thermal imbalance that will return the system to the equilibrium point (Fig. 2) [24, 45, 48]. At this stable equilibrium, a magma ocean can maintain a relatively constant temperature. The LMO will leave the stable equilibrium once tidal heating begins to diverge from the cooling rate, corresponding to the high-viscosity branch of the heating curve, which has a negative slope. This is an unstable equilibrium point, at which further cooling causes a rapid decrease (instead of increase) in tidal heating. At this point, cooling and solidification will proceed rapidly (Fig. 2). A fundamental and persistent property of tidally heated magma oceans is that they spend most of their evolution at a series of stable points, followed by rapid transitions to lower-temperature stable states, with little time spent in the transition states [45]. This behavior appears to be consistent with the geochronologic observations of LMO products, both the delay and

the rapid final solidification. Such tidal heating models have been applied to Io, icy moons and the Earth [15, 24, 29, 30, 37, 45], but to our knowledge have not been applied to the LMO.

To test the efficacy of LMO tidal heating, we developed a coupled thermal–orbital evolution model for the early Moon (4.50–4.00 Ga) to evaluate tidal dissipation within the LMO itself. We show that a high-energy thermal plateau (stable equilibrium) followed by a thermal cliff (rapid transition between stable states) emerges as a robust, intrinsic property of a tidally heated LMO. Moreover, the model predicts stronger tidal heating on the nearside than the farside, consistent with asymmetric solidification of the LMO [3, 44, 57], and observations of nearside–farside dichotomies in composition [12, 22, 23, 52, 61, 63], crustal thickness [2, 40, 58], and rheology [41].

Results

For the time interval of interest (4.50–4.00 Ga), the radiogenic heating rate (\dot{E}_{rad}) from long-lived isotopes in the mantle is $\sim 1.8\text{--}1.4$ TW (1 TW = 10^{12} W) (Fig. S2). We define enhanced tidal heating to be when the tidal heating rate (\dot{E}_{tidal}) exceeds the radiogenic baseline. The high-energy thermal plateau occurs when $\dot{E}_{\text{tidal}} > \dot{E}_{\text{rad}}$. The first time \dot{E}_{tidal} rises above \dot{E}_{rad} is t_i , and t_{cliff} is the time when \dot{E}_{tidal} drops back below \dot{E}_{rad} , i.e., the thermal cliff age. A suite of LMO thermal-budget evolutions under varying eccentricities and Earth–Moon distance histories is presented in the Supplementary Materials. Here we use a conservative baseline case in Fig. 1A—constant and relatively low eccentricity $e = 0.05$ and $Q_E/k_{2E} = 400$ (Earth’s quality factor over degree-2 Love number)—to illustrate the common features. The evolution separates naturally into four stages:

(1) *Early rapid cooling* — an initial state where tidal heating is negligible. Immediately after 4.50 Ga, the LMO cools rapidly; within 1 Myr (actual value 0.14 Myr), it drops to a bulk melt fraction (ϕ) of 0.57, with convective heat loss exceeding ~ 500 TW. During this interval, \dot{E}_{tidal} is at least an order of magnitude smaller than \dot{E}_{rad} (the left dashed tail in Fig. 1A), because the system has not yet reached the stable equilibrium point.

(2) *Stable equilibrium* — as temperature and melt fraction enter the transitional rheology window, tidal dissipation rises to the hundreds-of-TW level, until it equals the cooling rate. With continued lunar recession, the tidal heating curve lowers (red curves in Fig. 2), and the equilibrium point shifts to lower melt fractions and temperatures, until it reaches the peak of the tidal heating curve (critical melt fraction of 30–50%).

(3) *Thermal cliff* — near 4.35 Ga (actual value 4.348 Ga at $\phi = 0.22$), the relative slope of the heating curve reverses, and the equilibrium becomes unstable. Further cooling lowers the tidal heating rate, causing even more cooling. \dot{E}_{tidal} drops below \dot{E}_{rad} rapidly, within < 30 Myr.

(4) *Secular slow cooling* — after t_{cliff} , tidal heating is low, total cooling is buffered primarily by radiogenic heating and a new stable state is reached.

The cases in the Supplementary Materials generally exhibit all four stages, with all the t_i occurring within ~ 1 Myr of lunar formation. However, the subsequent amplification of tidal heating and t_{cliff} varies with parameter choices. Owing to the early small Earth–Moon distance, the terminal tidal heating just prior to the thermal cliff (the end of stage 2) is usually high, > 10 TW. Thus, the plateau height is sufficient to dominate the thermal budget over \dot{E}_{rad} (~ 1.8 TW). For the cliff ages, as shown in Fig. 3, t_{cliff} shifts with orbital parameters: larger eccentricities and a smaller Earth–Moon distance (higher Q_E/k_{2E}) strengthen tidal forcing and extend the high-dissipation state. Across the explored ranges of eccentricity and Earth–Moon distance, t_{cliff} spans $\sim 4.50\text{--}3.50$ Ga. The dashed curves in Fig. 3 show that multiple combinations of eccentricity and Earth–Moon

distance can yield t_{cliff} within 4.35 ± 0.05 Ga. Further discussion of parameter sensitivities is provided in the section below and in the Supplementary Materials.

In our baseline case, the forcing distance is the center-to-center Earth–Moon separation. We also explored nearside–farside differences within the same framework by treating the nearside and farside as small radial offsets of $\pm R_M$ from the lunar center and using a Taylor expansion of Earth’s gravity to evaluate the near–far ratio of tidal forcing, which we then apply as a hemispheric weighting on the tidally dissipated power (see Methods, §2.5). The resulting tidal heating and temperature trajectories are shown in Figs. 4 and S8. During the stable equilibrium period, the temperature difference between the nearside and farside is minimal (< 5 °C). However, the farside reaches the unstable point earlier than the nearside. In the timespan between when the farside and nearside reach the unstable equilibrium point, the temperature difference rises dramatically. Within the range of parameters explored here, the peak temperature differences are 20 to 100 °C and last for 10 to over 100 Myr. For cliff ages of 4.4–4.3 Ga, the temperature difference is 20–60 °C, and the time interval is 10–20 Myr. The calculations are zero-dimensional and so do not fully capture the complexity of asymmetric tidal heating [44], and so the result should be taken as semi-quantitative, indicating just that the nearside and farside should experience a short period of increased temperature difference when they reach the unstable equilibrium point (thermal cliff). Additional discussion about asymmetric crystallization is provided in Discussion §3.

Discussion

Tidal heating as a major heat source of the LMO

Through the thermal plateau, tidal heating exceeds 500 TW initially and remains > 30 TW by ~ 4.35 Ga, whereas radiogenic heating starts near 1.8 TW and declines slowly. Thus, throughout the LMO’s pre-solidification epoch, tidal dissipation typically outpaces radiogenic production by more than an order of magnitude. Hence, a direct implication of our results is that tidal heating was likely to have been a primary heat source for the LMO. This conclusion is consistent with prior work on Io, icy bodies, exoplanets, and Earth [24, 45, 54], which shows that dissipation can rise by orders of magnitude in a transitional regime between the purely liquid and purely solid limits.

We now outline the physical mechanism showing that this behavior is an inherent property of a tidally heated magma ocean. The essence can be captured by the dimensionless forcing parameter $\chi \equiv \omega\tau$ [14, 15], where ω is the dominant tidal frequency and τ is the viscoelastic relaxation time. Tidal dissipation rises sharply when $\chi \approx 1$ (see explanations below). As for the various stages in the magma ocean’s evolution: (1) *Liquid-like limit* ($\chi \ll 1$): the forcing is slow relative to relaxation. The body flows easily—strain is large, but stress is small and quickly relaxed, so the stress–strain loop is narrow, leading to low dissipation. (2) *Solid-like limit* ($\chi \gg 1$): the forcing is fast relative to relaxation. The body is stiff within a cycle—stress is large, strain is small, and little mechanical work is irreversibly lost per cycle, also leading to low dissipation. (3) *Transitional regime* ($\chi \approx 1$): both stress and strain are appreciable within each cycle, maximizing the stress–strain loop area (work done per cycle), and enhancing tidal dissipation. This is the enhanced tidal heating window that sustains the thermal plateau. For lunar conditions, our simple estimate (see Fig. S3 in the Supplementary Materials) indicates that the dissipation peak occurs at viscosities of 10^{12} to 10^{16} Pa s. Therefore, as the LMO evolves from a nearly pure melt (< 1 Pa s) to a largely solid state ($> 10^{20}$ Pa s), it will inevitably pass through the viscosity window in which tidal heating

peaks. This transitional regime has been investigated experimentally for silicate systems [34], with the onset typically associated with a melt fraction of ~ 0.4 ; in reality, the viscosity peak can occur over a broader range of ~ 0.2 – 0.6 .

Delayed and rapid final solidification of the LMO

The narrow band of ages observed for LMO crystallization products suggests that some heat source maintained the LMO in a highly molten state for over 100 Myr, before the final 30–50% crystallized rapidly [8–10]. This is not explained by convective cooling models in which radiogenic heating is the main heat source [17, 46]. However, such thermal plateaus, followed by rapid cooling, are robust features of tidally heated magma oceans [24, 45, 48]. Our models demonstrate that a range of orbital and rheologic values are consistent with the rapid solidification of the final $< 50\%$ of the LMO occurring around 4.35 Ga (Figs. 3 and S6). Even models with very conservative choices of eccentricity and Q_E/k_{2E} produce the requisite tidal heating. The tidally heated LMO model does not require special orbital circumstances, instead simply calling on the steady cooling of the magma ocean and a non-zero orbital eccentricity.

The tidal heating model does require some portion of the LMO to maintain intermediate melt fractions (~ 0.2 – 0.6) over tens of millions of years. Crystal settling and compaction can be rapid when the density difference between the melt and solid are substantial. However, in both the early and late stages of LMO solidification, solid–melt density differences could be small, and convective forces could have maintained the requisite melt fractions over large portions of the LMO. In general, crystal settling and matrix compaction reduce tidal heating by shrinking the volume of the LMO at or around transitional melt fractions; however, when inertial tidal resonances are considered, compaction can shift the resonance frequencies upward, enhancing dissipation at those shifted frequencies [30]. In the Supplementary Materials, we explore models in which only a fraction of the LMO is tidally heated and show that while this changes the specific parameter values that can produce the thermal cliff at 4.35 Ga (Fig. S7), it does not change the primary conclusions of this study (see Supplementary Materials for discussion).

Asymmetric crystallization of the LMO

As discussed above, tidal heating of the LMO should be asymmetric and should maintain a 30–60 °C temperature difference between the nearside and farside for tens of millions of years. The nearside/farside thermal gradient would induce asymmetric crystallization of the LMO. Several previous studies have hypothesized asymmetric crystallization based on the localization of the KREEP component and mare volcanism on the nearside, the apparent crustal thickness dichotomy [57, 58] and remotely sensed Mg# of anorthositic crust [40, 52]. In the tidal heating model, the first stage of LMO crystallization would take place prior to, and during, the stable equilibrium period, during which the temperature difference between the nearside and farside is minimal (Fig. 4). The LMO stays in this state until the melt fraction reaches the critical melt fraction (Fig. 2), somewhere between 30 and 50% melt. Therefore, for the first 50–70% of LMO crystallization, temperature differences between the nearside and farside would have been small, and the early (pre-4.3 Ga), mafic cumulates should be similar in composition on the nearside and farside, consistent with the similarity of the depleted isotopic endmembers in nearside and farside samples (see Fig. 4, [63]).

Our model implies that the farside anorthositic crust should have crystallized a few tens of

millions of years earlier, on average, than the nearside crust, and from a less fractionated, higher-Mg# LMO (Fig. 4). Experimental studies on LMO crystallization [47] indicate that a 40–60 °C difference in late-stage plagioclase+pyroxene crystallization should produce a ~ 10–15 Mg# difference in the pyroxenes, consistent with the variation seen in remotely sensed data [40] and in lunar anorthositic meteorites [20]. The last 5–10% of the LMO should have largely crystallized on the nearside. This is consistent with the concentration of KREEP and high Fe–Ti components on the nearside [3, 40, 57]. There is evidence for some KREEP-like material on the farside from the distribution of Th associated with SPA and elevated trace elements in Chang’e 6 samples [12, 23, 51, 60, 63]. This could indicate that sweeping of the last dregs of the LMO to the nearside was not 100% efficient, perhaps due to heterogeneities in crust/lithosphere thickness and in the distribution of tidal heating. Concentration of incompatible elements on the nearside, including H₂O and Fe₂O₃, may also provide an explanation for the observed nearside/farside difference in water content and oxygen fugacity, respectively [41, 60]. Further 2D and 3D modeling of an asymmetrically heated, crystallizing LMO will be needed to fully explore the generation of these asymmetries.

Our results imply that tidal heating exerted a primary control on LMO evolution. The observed > 100 Myr delay of LMO crystallization, followed by rapid final solidification, appears to be an example of punctuated, nonlinear behavior inherent to tidal heating, producing thermally stable eras separated by short, rapid transitions. Asymmetry in LMO tidal heating could also have caused the many nearside/farside dichotomies observed in the Moon. In addition to the LMO, recent models [62] have revived the idea that tidal heating (of a solid Moon) could be the heat source for mare volcanism after ~ 4 Ga [28]. If so, tidal heating appears to have been a long-lived driver of the Moon’s igneous evolution.

Acknowledgments

We thank Greg Hirth, Reid Cooper, Christian Huber, and Marc Parmentier for helpful discussions.

Funding: This work was supported by the LunaSCOPE NASA SSERVI node (grant 80NSSC23M0161).

Author contributions: Conceptualization: W.Z., S.P., H.L., and J.W.H. Methodology: W.Z. and H.L. Software: W.Z. and H.L. Formal analysis: W.Z. and H.L. Investigation: W.Z. and H.L. Visualization: W.Z., S.P., and H.L. Funding acquisition: S.P., H.L., and J.W.H. Supervision: H.L., S.P., and J.W.H. Writing – original draft: W.Z. and S.P. Writing – review & editing: W.Z., H.L., S.P., and J.W.H.

Competing interests: The authors declare that they have no competing interests.

Data and materials availability: All data needed to evaluate the conclusions in this paper are present in the main text and the Supplementary Materials. The model code required to reproduce the results has been provided to the editors and reviewers as part of the submission. The code will be made publicly available upon acceptance.

Supplementary materials

Materials and Methods

Supplementary Text

Figs. S1 to S8

Table S1

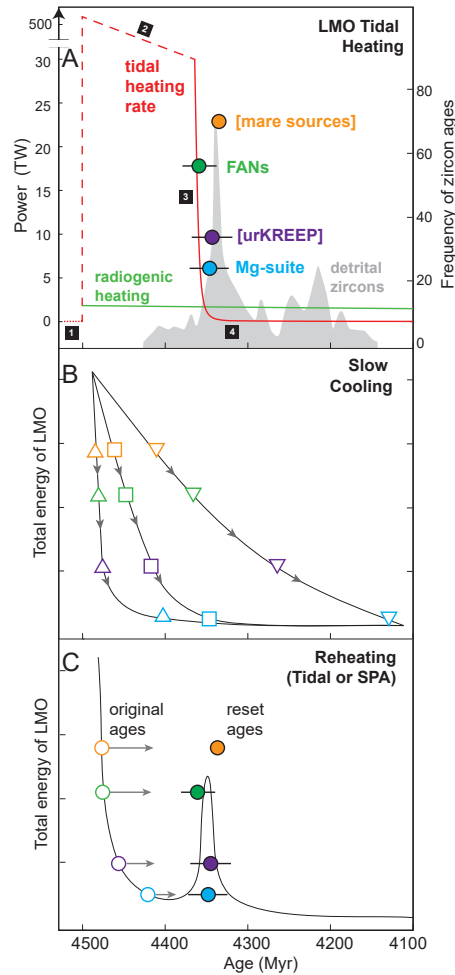


Figure 1: LMO crystallization geochronology predicted by different thermal evolution models. (A) Ages of mare-basalt mantle sources (pyroxenites, orange), Ferroan Anorthosites (FANs, green), urKREEP (purple), and Mg-suite rocks (blue) cluster near ~ 4.35 Ga. These represent the last 30–50% of LMO solidification and post-solidification overturn (Mg-suite). The light-gray curve shows the age distribution of early detrital zircons, which also peaks at ~ 4.35 Ga. Data are from Borg and Carlson (2023) [8] and references therein. The red curve shows the modeled LMO tidal-heating rate, featuring a prolonged thermal plateau followed by a thermal cliff at ~ 4.35 Ga. The green near-horizontal curve indicates the radiogenic heating rate for comparison. White numerals in black squares mark stages 1–4 of the LMO thermal evolution. **(B)** End-member cooling histories with different total cooling rates. A fast-cooling case (leftmost curve) produces clustered ages but much older ages than observed, whereas slower cooling (right two curves) extends LMO solidification and yields a more dispersed age distribution than observed. **(C)** In reheating models, the LMO solidifies early, and a later post-solidification event (e.g., the South Pole–Aitken (SPA) impact or the Laplace Plane Transition (LPT) event) reheats and resets the ages of all LMO products. Symbols in panels (B) and (C) match the four lithologies and colors in panel (A).

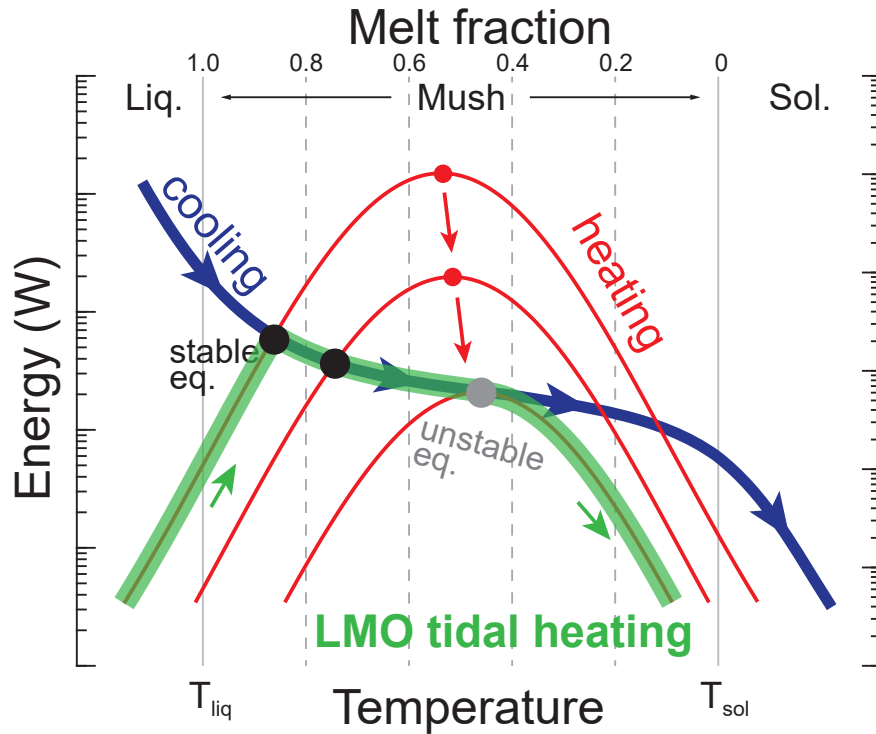


Figure 2: **Tidal heating evolution of the LMO.** Coevolution of LMO temperature, tidal heating, and total energy. Temperature on the lower axis decreases from left to right; two vertical gray lines mark the liquidus and solidus. The upper axis shows melt fraction, partitioning the diagram into liquid, mush, and solid regimes. Energy (watts) is plotted on a logarithmic scale. The blue curve is total cooling power (convection + conduction). The red curves are tidal-heating power for different assumed Earth–Moon distances. The red arrows show that as the Earth–Moon distance increases, the peak tidal-heating power (red dots) decreases. The green curve traces the tidal heating rate within the LMO. Tidal power is small at very high and very low temperatures and rises by orders of magnitude across the rheological transition, peaking near an intermediate melt fraction of ~ 0.4 . Because the initial energy is high, the LMO cools rapidly at first. It then enters a regime where tidal heating and cooling nearly balance; intersections of the red and blue curves (black points) are stable equilibria, and the system moves through a sequence of these as tidal power wanes with increasing Earth–Moon distance. The sequence ends at a tangency (gray point), an unstable equilibrium. Between the first stable intersection and this unstable tangency, strong tidal heating buffers energy loss, producing a gentler net-cooling slope—a high-energy plateau in the LMO’s evolution. Beyond the unstable point, tidal power collapses, total cooling exceeds heating, and the system descends a sharp cliff.

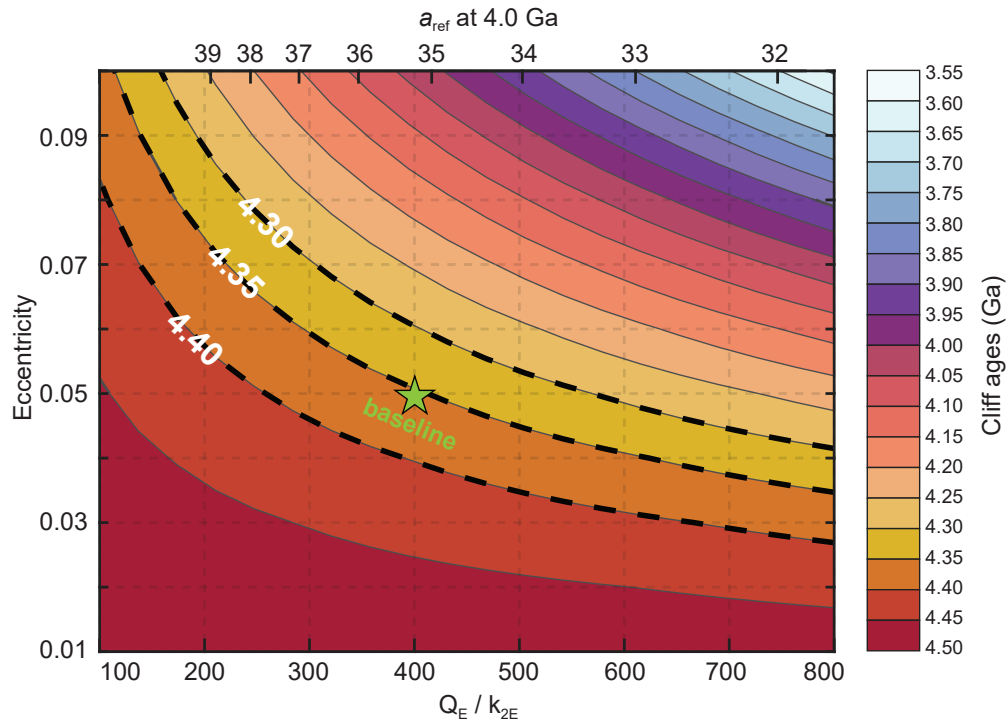


Figure 3: **Duration of LMO tidal heating as a function of eccentricity and Earth’s tidal parameters.** The x-axis is Earth’s tidal quality factor over Love number, Q_E/k_{2E} , which varies inversely with the rate of Earth–Moon distance expansion; the y-axis is the lunar orbital eccentricity e . The color map gives the “cliff age”—the first time at which LMO tidal heating drops below radiogenic heating following the high-energy plateau—and thus scales inversely with the duration of the high tidal-heating interval. Three dashed curves mark contours at cliff ages of 4.40, 4.35, and 4.30 Ga. The corresponding $(e, Q_E/k_{2E})$ combinations along these contours are, to first order, consistent with the available geochronological constraints on sample ages. The green star denotes the parameter choice used in Fig. 1A ($e = 0.05, Q_E/k_{2E} = 400$), consistent with prior early Earth–Moon distance evolution models [18].

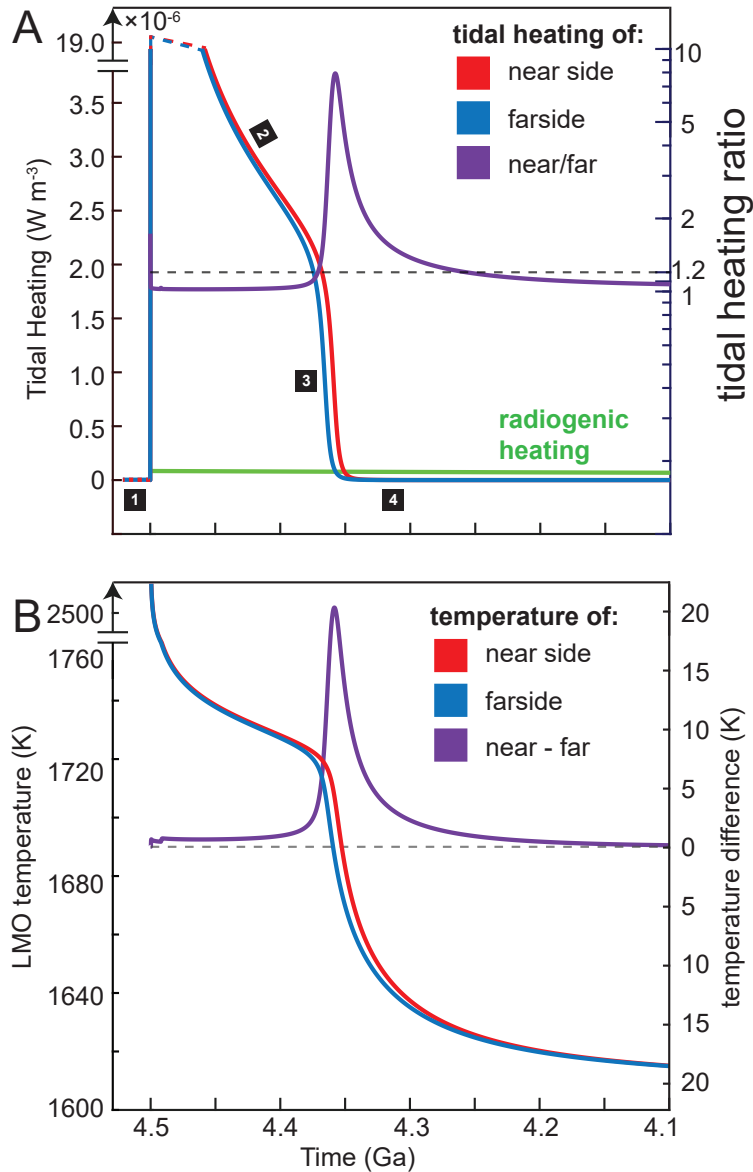


Figure 4: Asymmetric tidal heating of the LMO. Tidal heating rates for the lunar nearside and farside are computed by perturbing the tidal amplitude (for methods, see the Supplementary Materials) relative to the baseline case in Fig. 1A. Other parameters, such as eccentricity and viscosity are held fixed. **(A)** Tidal-heating histories for the nearside (red) and farside (blue). The curves track closely through stable-equilibrium stage 2, then diverge as the farside reaches the unstable equilibrium earlier because its forcing distance is larger ($+R_M$). The nearside-to-farside tidal-heating ratio (purple, right axis) is shown with a dashed reference line at 1.2. The ratio peaks at 7.9 at 4.36 Ga; at most other times before 4.35 Ga, it remains ≤ 1.2 . **(B)** Temperature evolution. The temperature difference between the nearside and farside is minimal during the stable-equilibrium stage 2, and peaks in the time between the farside and nearside reaching the unstable point. The purple curve shows $T_{\text{near}} - T_{\text{far}}$, peaking at $\sim 20^\circ\text{C}$ near 4.35 Ga. White numerals in black squares mark stages 1–4 of the LMO thermal evolution. Results based on additional orbital parameter choices can be found in the Supplementary Materials.

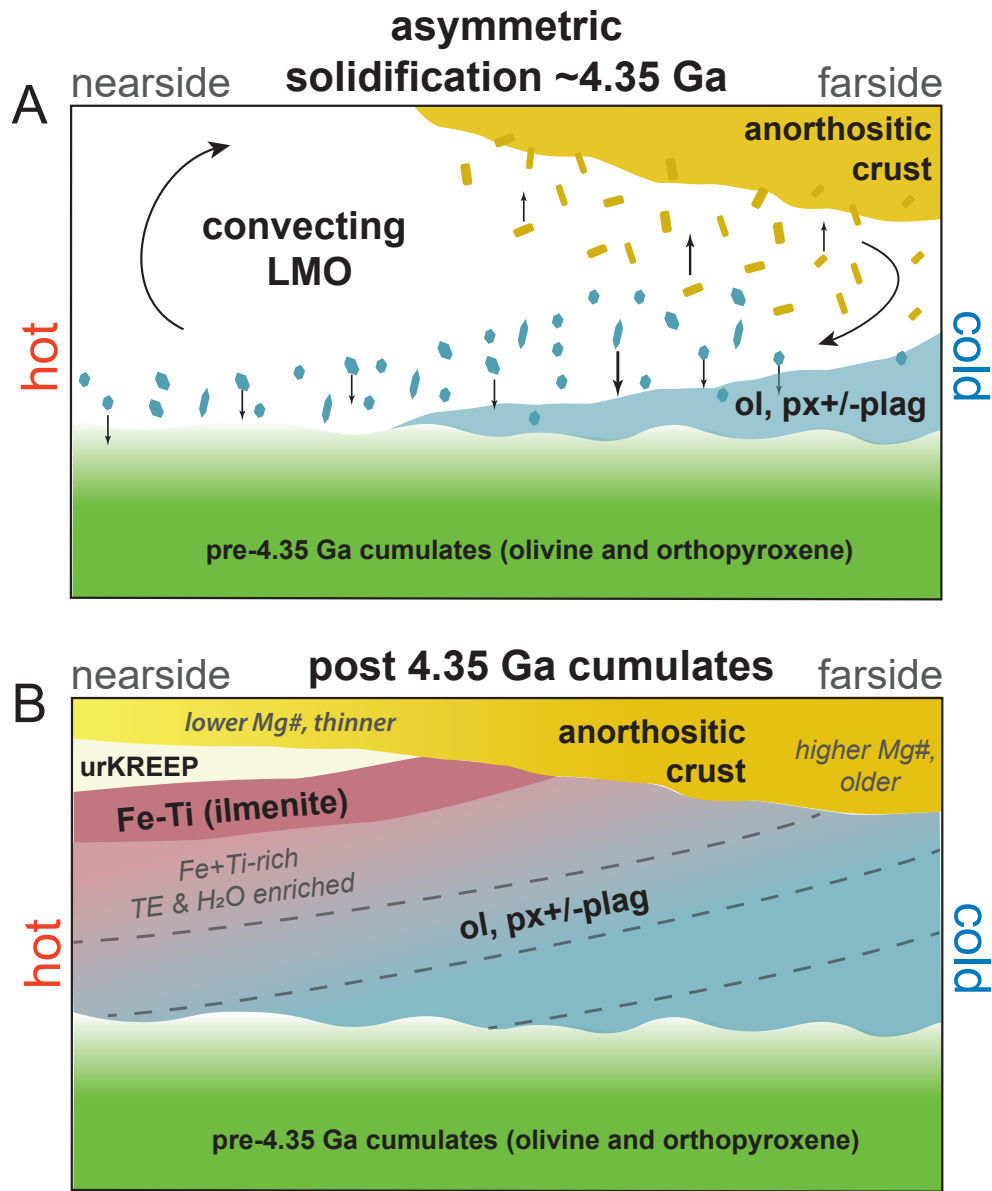


Figure 5: **Asymmetric crystallization of the LMO driven by differential tidal heating.** (A) Nearside-hot / farside-cold state at ~ 4.35 Ga, just as the farside has passed the unstable point and is cooling rapidly. Enhanced tidal/thermal input on the nearside keeps the LMO warmer and delays the plagioclase flotation process there, while the farside cools faster and forms a thicker, earlier anorthositic crust. Early mafic cumulates (olivine ± orthopyroxene) deposited before ~ 4.35 Ga are compositionally similar on both sides. (B) Post-4.35 Ga cumulates. Continued crystallization and asymmetric cooling concentrate late Fe–Ti–rich melts and urKREEP beneath the thinner nearside crust, enriching the nearside in Fe, Ti, incompatible elements, and H₂O. The farside retains older, higher-Mg# anorthosite and thicker crust; dashed horizons schematically illustrate the nearside-ward tilting of mafic cumulates. Figure is not to scale.

The Supplementary Materials comprise two sections. Materials and Methods details the modeling framework, and Supplementary Text presents additional modeling results across a range of parameter values together with further discussions.

Materials and Methods

The main objective of our model is to estimate the tidal heating within the silicate portion of the Moon following its initially molten state—the so-called Lunar Magma Ocean (LMO)—to shortly after its solidification. Accordingly, our approach follows previous formulations that calculate tidal heating over the full magma ocean life cycle for other bodies. Such models have been developed for Io and exoplanets [15, 18, 24, 37, 45, 54], as well as for Earth [29–32, 59]. For the Moon, there have also been studies related to tidal heating targeting the earliest epoch (~ 4.5 – 4.0 Ga), but these works emphasized possible tidal reheating events after solidification of the LMO [17, 38], rather than dissipation within the magma ocean during its evolution. Hence, to our knowledge, the present study is the first to explicitly simulate tidal heating inside the LMO itself.

We adapt parameterized Io/exoplanet frameworks [24, 25, 45] to the Moon and solve for the thermal evolution of the LMO within the context of the Earth–Moon system. The geometry of the model is summarized in Fig. S1. We represent the LMO as a homogeneous layer with uniform temperature and bulk properties. Energy exchange is mediated by parameterized boundary layers at the surface (radiative/advective coupling to space) and at the core–LMO interface (basal heat exchange). All parameter values used in this study are listed in Table S1. Given the huge uncertainties in the initial conditions of the LMO and parameters involved, it is reasonable to keep our model simple in order to demonstrate the feasibility of our proposed mechanism in prolonging the existence of the LMO.

1. Energy balance of the LMO

In our thermal evolution framework, the LMO gains energy from tidal dissipation, radiogenic decay of long-lived nuclides, and possible heat inflow from the core, and it loses energy via convective heat transport eventually lost through its surface. The net energy budget is

$$\dot{E}_{\text{LMO}} = \dot{E}_{\text{tide}} + \dot{E}_{\text{rad}} + \dot{Q}_{\text{CMB}} - \dot{Q}_{\text{conv}}, \quad (\text{S1})$$

where \dot{E}_{LMO} , \dot{E}_{tide} , \dot{E}_{rad} , \dot{Q}_{CMB} , and \dot{Q}_{conv} are the rates of change of the LMO’s internal thermal energy, tidal heating within the LMO, radiogenic heating from long-lived isotopes, the net heat flow into the LMO across the core–mantle boundary (CMB), and the convective heat loss from the LMO to the surface.

The coupled evolution of the LMO mean temperature T_m and the core temperature T_c follows energy conservation within each reservoir. For the LMO,

$$\frac{dT_m}{dt} = \frac{\dot{E}_{\text{LMO}}}{C_{\text{LMO,eff}}} = \frac{\dot{E}_{\text{rad}} + \dot{E}_{\text{tide}} + \dot{Q}_{\text{CMB}} - \dot{Q}_{\text{conv}}}{C_{\text{LMO,eff}}}, \quad (\text{S2})$$

where $C_{\text{LMO,eff}}$ is the LMO’s effective heat capacity that accounts for latent-heat buffering during crystallization,

$$C_{\text{LMO,eff}} = M_{\text{LMO}} c_{\text{LMO}} (1 + \text{Ste}^{-1}), \quad \text{Ste} = \frac{c_{\text{LMO}} (T_l - T_s)}{L_{\text{LMO}}}. \quad (\text{S3})$$

Here, M_{LMO} and c_{LMO} are the LMO mass and specific heat, L_{LMO} is the latent heat of fusion, and T_l and T_s are the liquidus and solidus temperatures, respectively. We adopt $L_{\text{LMO}} = 3.2 \times 10^5 \text{ J kg}^{-1}$ [49]. Ste is the Stefan number—i.e., the ratio of sensible heat to latent heat—so that $c_{\text{LMO,eff}} = c_{\text{LMO}} + L_{\text{LMO}}/(T_l - T_s)$.

The core cools through exchange with the LMO across the CMB, which we model as

$$\frac{dT_c}{dt} = -\frac{\dot{Q}_{\text{CMB}}}{M_c c_c}, \quad (\text{S4})$$

where T_c is the core temperature (assumed to be well mixed), M_c the core mass, c_c its specific heat, and \dot{Q}_{CMB} the net heat flow across the CMB. We adopt the sign convention $\dot{Q}_{\text{CMB}} > 0$ for heat flowing from the core into the LMO.

Simulations begin with initial conditions of $T_m(t_0) = 3000 \text{ K}$ and $T_c(t_0) = 3100 \text{ K}$. We find that our simulations are relatively insensitive to this choice (both the absolute values and the difference between T_m and T_c , see Section 3.1). In the subsections below, we detail the calculations of the surface radiogenic loss \dot{E}_{rad} , the CMB exchange \dot{Q}_{CMB} , and the convective transport \dot{Q}_{conv} . Section 2 presents the tidal-heating formulation, \dot{E}_{tide} .

1.1 Radiogenic heating calculation

Radiogenic heating in the LMO is modeled as the combined contribution of the four dominant long-lived isotopes, ^{232}Th , ^{238}U , ^{235}U , and ^{40}K . The total radiogenic power of the mantle at time t is

$$\dot{E}_{\text{rad}}(t) = M_{\text{LMO}} \sum_{i=1}^4 H_i C_i \exp[\lambda_i (T_{\text{tot}} - t)], \quad (\text{S5})$$

where H_i , C_i , λ_i , T_{tot} , and t are the present-day specific heat production of isotope i , the present-day bulk concentration of isotope i in the LMO, the decay constant (where $\lambda_i = \ln 2/t_{1/2,i}$, with half-life $t_{1/2,i}$), total time since lunar formation (i.e., $T_{\text{tot}} = 4.5 \text{ Gyr}$), and t is the model time, respectively. Fig. S2 shows the 4.5-billion-year evolution of radiogenic heating rates in Earth and the Moon. Notably, Earth's radiogenic output declines from $\sim 75 \text{ TW}$ at $t = 0$ to $\sim 18\text{--}20 \text{ TW}$ at $t = 4.5 \text{ Gyr}$, whereas the Moon's radiogenic output drops from $\sim 1.8 \text{ TW}$ to $\sim 0.4\text{--}0.5 \text{ TW}$ (Fig. S2). In comparison, the Moon's absolute level of radiogenic power is modest and its variation over time comparatively small. Over the window emphasized in this study (4.5–4.0 Ga), Earth's radiogenic power decreases from ~ 75 to $\sim 60 \text{ TW}$, while the Moon's decreases from ~ 1.8 to $\sim 1.4 \text{ TW}$. Relative to the larger magnitude and variability of the tidal heating we simulate below, radiogenic heating can be viewed as quasi-constant over this interval.

1.2 Convective heat loss and core-mantle boundary heat flux

Following [45, 49], we treat the LMO as bounded by two thermal boundary layers: an upper boundary layer (UBL) beneath the surface and a lower boundary layer (LBL) coincident with the CMB. The UBL sets the convective heat loss to space and is the dominant cooling pathway, whereas the LBL regulates the upward core heat flux. We determine boundary-layer thicknesses and fluxes using Nusselt number–Rayleigh number (i.e., Nu and Ra) scalings.

Upper boundary layer. The UBL thickness δ_u is related to the Nusselt number via

$$\text{Nu}_u = a_c \left(\frac{\text{Ra}_u}{\text{Ra}_c} \right)^{1/3}, \quad \delta_u = \frac{D_m}{2 \text{Nu}_u}, \quad (\text{S6})$$

with calibration constants $a_c \approx 0.1$ and critical Rayleigh number $\text{Ra}_c \approx 1100$. The UBL Rayleigh number, Ra_u , uses LMO-average properties and the following temperature drop ($T_m - T_{\text{surf}}$):

$$\text{Ra}_u = \frac{\rho g \alpha_T (T_m - T_{\text{surf}}) D_m^3}{\kappa \eta_u}, \quad (\text{S7})$$

where ρ is density, g gravity, α_T thermal expansivity, D_m LMO thickness, κ thermal diffusivity, and η_u the effective viscosity in the UBL. The conductive flux through the UBL is

$$F_{\text{conv}} = \frac{k_m (T_m - T_{\text{surf}})}{\delta_u} = \text{Nu}_u \frac{2k_m (T_m - T_{\text{surf}})}{D_m}, \quad (\text{S8})$$

and so the total convective power is

$$\dot{Q}_{\text{conv}} = 4\pi R_M^2 F_{\text{conv}}. \quad (\text{S9})$$

We cap $\text{Nu}_u \leq \text{Nu}_{\text{max}}$ and take $\text{Nu}_{\text{max}} = 10^5$ to avoid unrealistically thin (centimeters to meters) UBL thickness during the early low-viscosity stage.

Lower boundary layer (CMB). At the base, the LBL thickness δ_ℓ controls the CMB heat exchange. We scale δ_ℓ to δ_u using a viscosity–contrast parameterization [38, 49]:

$$\delta_\ell = \frac{\delta_u}{2} \left[\gamma (T_c - T_m) \right]^{-1/3} \exp\left(-\frac{\gamma (T_c - T_m)}{6} \right), \quad (\text{S10})$$

where $\gamma \approx 0.011 \text{ K}^{-1}$ controls the effective viscosity contrast across the CMB. This yields thinner LBLs for larger $(T_c - T_m)$ while limiting unrealistically large contrasts. The corresponding CMB total heat flux is

$$\dot{Q}_{\text{CMB}} = 4\pi R_c^2 \frac{k_m (T_c - T_m)}{\delta_\ell}, \quad (\text{S11})$$

with R_c the core radius, k_m the mantle's thermal conductivity, and $\dot{Q}_{\text{CMB}} > 0$ denoting heat flowing from the core into the LMO.

Surface boundary condition. We approximate the instantaneous surface temperature as a gray-body balance between the globally averaged absorbed insolation and the interior heat release,

$$T_{\text{surf}}^4 = \frac{1}{\epsilon_v \sigma_B} \left[\frac{(1 - A) L_\star}{16\pi a_\star^2} + \frac{\dot{Q}_{\text{conv}}}{4\pi R_M^2} \right], \quad (\text{S12})$$

where A is Bond albedo, L_\star stellar luminosity, a_\star heliocentric distance, ϵ_v emissivity, σ_B the Stefan–Boltzmann constant, and R_M is the radius of the Moon.

In summary, Eqs. (S6)–(S12) couple LMO convection, CMB exchange, and radiative cooling: the boundary layers set the efficiency of heat transfer, with \dot{Q}_{conv} governing outward LMO cooling and \dot{Q}_{CMB} regulating core–LMO exchange.

2. Tidal heating in the LMO

We compute the LMO tidal heating using a simplified viscoelastic Love-number formalism, in which the imaginary part of the degree-2 Love number, $-\Im[k_2(\omega)]$, quantifies dissipation within the LMO. For a synchronously rotating Moon on an eccentric orbit about Earth, the global tidal power is [48]

$$\dot{E}_{\text{tide}} = f_{\text{tvf}} \frac{21}{2} [-\Im(k_2(\omega))] \frac{G M_E^2 R_M^5}{a_{E-M}^6} n e^2, \quad (\text{S13})$$

where G is the gravitational constant, M_E the Earth's mass, a_{E-M} the Earth–Moon semi-major axis, e the orbital eccentricity, and n is the mean motion (defined below). The factor f_{tvf} accounts for the tidal-volume fraction—the fraction of the Moon's volume that participates in dissipation [24, 45]. We adopt an eccentricity of $e = 0.05$ as a conservative choice; additional cases are explored in Section 3.2.

$$n \equiv \sqrt{\frac{G M_E}{a_{E-M}^3}}. \quad (\text{S14})$$

As a baseline assumption, we take tidal dissipation to occur throughout the entire silicate portion above an undissipative core of radius R_c , which yields

$$f_{\text{tvf}} = \left[1 - \left(\frac{R_c}{R_M} \right)^3 \right] \phi(T_m), \quad (\text{S15})$$

where $\phi(T_m)$ is the volume-averaged melt fraction of the LMO, used here as a proxy for the fraction of the silicate shell that remains in a connected magma-ocean/mush state and can participate efficiently in tidal dissipation. In practice, the fraction of tidal power actually generated is likely smaller than the full-silicate-portion value; we revisit this point in Section 3.3.

2.1 Imaginary part of the Love number

The dissipation is governed by the negative imaginary part of the degree-2 Love number, $-\Im(k_2)$, which encapsulates the frequency-dependent lag between forcing and response. Following [15],

$$-\Im(k_2) = -\frac{3}{2} \frac{J_U \tilde{\mu} \Im(\bar{J})}{[\Im(\bar{J})]^2 + [\Re(\bar{J}) + J_U \tilde{\mu}]^2}, \quad (\text{S16})$$

where $\bar{J}(\omega)$ is the complex compliance of the viscoelastic body, $J_U = 1/\mu_U$ is the unrelaxed (instantaneous) compliance set by the infinite-frequency shear modulus μ_U , and

$$\tilde{\mu} = \frac{19 \mu_U}{2 \rho g R_M} \quad (\text{S17})$$

is the (dimensionless) effective rigidity where ρ is bulk density and g surface gravity. Here, $\Re(\bar{J})$ and $\Im(\bar{J})$ denote the real and imaginary parts of the complex compliance \bar{J} , respectively. Physically, the real part describes elastic storage, whereas the imaginary part quantifies dissipation.

2.2 Complex compliance: Maxwell model for the LMO

We adopt a Maxwell rheology for the LMO, with complex compliance

$$\bar{J}_M(\omega) = J_U + \frac{1}{i\omega\eta_S} = J_U - i\frac{1}{\omega\eta_S}, \quad (\text{S18})$$

where η_S is the shear viscosity and ω is the principal tidal forcing frequency. Thus $\Re(\bar{J}_M) = J_U$ and $\Im(\bar{J}_M) = -1/(\omega\eta_S)$.

Substituting Eq. (S18) into Eq. (S16) yields a closed-form expression for the k_2 Love number:

$$-\Im(k_2)_M = \frac{3}{2} \frac{J_U \tilde{\mu}(\omega\eta_S)}{1 + [J_U(1 + \tilde{\mu}(\omega\eta_S))]^2}. \quad (\text{S19})$$

Equations (S13) and (S19) couple the orbital state (a, e, n) with the LMO rheology (μ_U, η_S, ρ, g) to give the time-dependent tidal power.

2.3 Transitional rheology parameterizations

(i) Melt fraction. Following [59], melt fraction is expressed as

$$\phi(T) = \begin{cases} 0, & T \leq T_{\text{sol}}, \\ \frac{T - T_{\text{sol}}}{T_{\text{liq}} - T_{\text{sol}}}, & T_{\text{sol}} < T < T_{\text{liq}}, \\ 1, & T \geq T_{\text{liq}}, \end{cases} \quad (\text{S20})$$

(ii) Shear modulus. Following [24], we adopt a three-piece liquidus-plateau form

$$\mu_U(T) = \begin{cases} \mu_0, & T \leq T_{\text{sol}}, \\ \mu_0 \exp\left(\frac{E_a}{R} \left[\frac{1}{T} - \frac{1}{T_{\text{sol}}}\right]\right), & T_{\text{sol}} < T < T_{\text{liq}}, \\ \mu_0 \exp\left(\frac{E_a}{R} \left[\frac{1}{T_{\text{liq}}} - \frac{1}{T_{\text{sol}}}\right]\right), & T \geq T_{\text{liq}}, \end{cases} \quad (\text{S21})$$

where μ_0 is the solidus reference modulus at $T_{\text{sol}} = 1600$ K, E_a is the activation energy, and R is the universal gas constant. This form is equivalent to $\mu_0 \exp(E_a/RT - C_0)$ with $C_0 = E_a/(RT_{\text{sol}})$.

(iii) Viscosity. As described in the main text, the essence of the enhanced tidal heating is that the dimensionless parameter $\chi \equiv \omega\tau$ is near unity ($\chi \approx 1$), where ω is the tidal forcing frequency and τ is the viscoelastic relaxation time. For lunar forcing frequencies this places the peak tidal-heating viscosity of the LMO at $\eta_S \sim 10^{12}$ – 10^{16} Pa s. Accordingly, we adopt a temperature-segmented parameterization with three anchor values: $\eta_{S,\text{sol}}^{\text{ref}}$, $\eta_{S,\text{cri}}^{\text{ref}}$, and $\eta_{S,\text{liq}}^{\text{ref}}$. These represent the shear viscosities at T_{sol} , T_{cri} , and T_{liq} , respectively; with default values used in our runs $\eta_{S,\text{sol}}^{\text{ref}} = 10^{19}$ Pa s, $\eta_{S,\text{cri}}^{\text{ref}} = 3.5 \times 10^{12}$ Pa s, $\eta_{S,\text{liq}}^{\text{ref}} = 10^{-3}$ Pa s. Thus, by tuning the viscosity near T_{cri} , we locate the tidal heating maximum within the transitional window at $\phi_c \approx 0.4$ (i.e., where $\chi \approx 1$).

Between these anchors, we parameterize the viscosity with an Arrhenius backbone augmented by a melt-weakening mechanism. Let A_ϕ be the weakening coefficient and set $\phi_s = 0$, $\phi_c = (T_{\text{cri}} - T_{\text{sol}})/(T_{\text{liq}} - T_{\text{sol}})$, $\phi_l = 1$.

The shear viscosity is prescribed as

$$\eta_S(T) = \begin{cases} \eta_{S,\text{sol}}^{\text{ref}} \exp\left[\frac{E_a}{R}\left(\frac{1}{T} - \frac{1}{T_{\text{sol}}}\right)\right], & T \leq T_{\text{sol}}, \\ \exp(a_1 + b_1 T^{-1}) \exp(-A_\phi \phi(T)), & T_{\text{sol}} < T \leq T_{\text{cri}}, \\ \exp(a_2 + b_2 T^{-1}) \exp(-A_\phi \phi(T)), & T_{\text{cri}} < T \leq T_{\text{liq}}, \\ \exp(a_2 + b_2 T_{\text{liq}}^{-1}) \exp(-A_\phi \phi_l), & T > T_{\text{liq}}, \end{cases} \quad (\text{S22})$$

where R is the gas constant and E_a is the activation energy for the low-temperature solid branch (no ϕ -weakening). The coefficients a_1, b_1 and a_2, b_2 are determined by the two-point constraints in each segment. This formulation ensures continuity at $T_{\text{sol}}, T_{\text{cri}}$, and T_{liq} , keeps the high-temperature branch constant at the (already weakened) value at T_{liq} , and reduces to a pure Arrhenius law below the solidus. In the numerics we cap η_S to $[\eta_{\text{min}}, \eta_{\text{max}}]$ with $\eta_{\text{min}} = 10^{-6}$ and $\eta_{\text{max}} = 10^{27}$ Pa s.

Peak viscosity. The dissipation efficiency is set by $-\Im[k_2(\omega)]$, whose Maxwell form is already given in Eq. (S19). Let $x \equiv \omega \eta_S$. Maximizing $-\Im[k_2]$ with respect to x yields

$$x_{\text{peak}} = \frac{1}{J_U (1 + \tilde{\mu})}, \quad \omega \tau_{\text{eff}} = 1, \quad \tau_{\text{eff}} = \frac{(1 + \tilde{\mu}) \eta_S}{\mu_U}, \quad (\text{S23})$$

and the corresponding peak value $-\Im[k_2]_{\text{peak}} = \frac{3}{4} \tilde{\mu}/(1 + \tilde{\mu})$. Hence the viscosity at which dissipation peaks is

$$\eta_{\text{peak}} = \frac{\mu_U}{(1 + \tilde{\mu}) \omega}. \quad (\text{S24})$$

In the rigid limit ($\tilde{\mu} \gg 1$) and using $\tilde{\mu} = 19\mu_U/(2\rho g R_M)$, Eq. (S24) reduces to the simple scaling

$$\eta_{\text{peak}} \approx \frac{2\rho g R_M}{19\omega}, \quad (\text{S25})$$

where all material and geometric parameters are as listed in Table S1. For a synchronously rotating Moon the principal forcing frequency is the mean motion, $\omega \simeq n(a) = \sqrt{GM_E/a^3}$ [Eq. (S14)], so that

$$\eta_{\text{peak}}(a) \approx \frac{2\rho g R_M}{19} \left(\frac{a^3}{GM_E}\right)^{1/2} \propto a^{3/2}. \quad (\text{S26})$$

With the lunar parameters in Table S1, $\eta_{\text{peak}}(a)$ over $a = 3\text{--}60 R_E$ lies in the transitional window targeted by our parameterization (order $10^{12}\text{--}10^{16}$ Pa s), and we illustrate this in Fig. S3 with a conservative $\times 10$ envelope reflecting uncertainty in frequency content and rheology.

2.4 Earth–Moon distance evolution

The secular evolution of the lunar semi-major axis $a(t)$ due to tides raised on the Earth is modeled with the constant $k_{2,E}/Q_E$ formulation following [36, 39]. The orbital recession rate is

$$\frac{da}{dt} = 3 \left(\frac{k_{2,E}}{Q_E} \right) \left(\frac{M_M}{M_E} \right) \left(\frac{R_E}{a} \right)^5 n(a) a, \quad (\text{S27})$$

where G is the gravitational constant, M_E , R_E , $k_{2,E}$, and Q_E are the Earth’s mass, radius, degree-2 tidal Love number, and tidal quality factor. M_M is the lunar mass and n is the mean motion defined in Eq. (S14). The initial semi-major axis is set to $a_0 = 3.0 R_E$, slightly beyond the Roche limit. In our baseline case we adopt constant values $k_{2,E} = 0.3$ and $Q_E = 120$, so that $Q_E/k_{2,E} = 400$. For the very early epoch considered here, Earth’s effective $k_{2,E}$ and Q_E are uncertain and could differ substantially from present-day values; a hotter, more deformable Earth could exhibit higher $k_{2,E}$ and higher Q_E (i.e., less dissipation per cycle). Using this constant ratio provides a simple, conservative baseline that yields an Earth–Moon distance history consistent with previous work [18], anchoring $a \approx 35 R_E$ at 4.0 Ga without invoking a closer initial configuration (Fig. S4). Additional Earth–Moon distance evolutions are examined in Section 3.2.

2.5 Nearside–farside tidal heating calculation

In our baseline symmetric model, the tidally dissipated power \dot{E}_{tide} depends on the center-to-center Earth–Moon distance a_{E-M} and the forcing frequency through Eqs. (S14) and (S13). For convenience we define a “baseline” tidal power at the lunar center,

$$\dot{E}_{\text{tide},0}(a_{E-M}, T_m) \equiv \dot{E}_{\text{tide}}(a = a_{E-M}, \omega = n(a_{E-M}); T_m), \quad (\text{S28})$$

where the rheology (and thus $-\mathfrak{J}[k_2]$) is evaluated using the local mantle temperature T_m , while the forcing frequency and Love number are always tied to the same center-to-center distance a_{E-M} .

To estimate the near–far asymmetry, we treat the nearside and farside as small radial offsets $\pm R_M$ from the lunar center along the Earth–Moon line. The Earth’s gravitational acceleration at radius r is

$$g(r) = \frac{GM_E}{r^2}, \quad (\text{S29})$$

and we write $r = a_{E-M}(1 + \delta)$ with $|\delta| \ll 1$. A Taylor expansion of $g(r)$ about $r = a_{E-M}$ gives

$$g(r) = \frac{GM_E}{a_{E-M}^2} (1 + \delta)^{-2} \approx g_0 (1 - 2\delta + 3\delta^2), \quad g_0 \equiv g(a_{E-M}) = \frac{GM_E}{a_{E-M}^2}, \quad (\text{S30})$$

where g_0 is the Earth’s gravitational acceleration at the lunar center. Defining the dimensionless finite-size parameter

$$\varepsilon_R \equiv \frac{R_M}{a_{E-M}}, \quad (\text{S31})$$

the nearside and farside correspond to $\delta_{\text{near}} = -\varepsilon_R$ and $\delta_{\text{far}} = +\varepsilon_R$, respectively. We note importantly that ε_R is time dependent and decreases significantly as a_{E-M} increases. Today, higher order terms of δ are ignored. Early in the Earth–Moon evolution, this is not the case. The local tidal acceleration

along the Earth–Moon line, which is proportional to the gradient of the tidal potential, is the difference between $g(r)$ and g_0 , so that, to second order in ε_R ,

$$\Delta g_{\text{near}} \equiv g(a_{\text{E-M}} - R_{\text{M}}) - g_0 \approx g_0(2\varepsilon_R + 3\varepsilon_R^2), \quad (\text{S32})$$

$$\Delta g_{\text{far}} \equiv g(a_{\text{E-M}} + R_{\text{M}}) - g_0 \approx g_0(-2\varepsilon_R + 3\varepsilon_R^2). \quad (\text{S33})$$

We factor out the leading-order (point-mass) tidal amplitude,

$$\Delta g_0 \equiv 2\varepsilon_R g_0, \quad (\text{S34})$$

and obtain, to first order in ε_R ,

$$\frac{\Delta g_{\text{near}}}{\Delta g_0} \approx 1 + \frac{3}{2}\varepsilon_R, \quad \frac{\Delta g_{\text{far}}}{\Delta g_0} \approx 1 - \frac{3}{2}\varepsilon_R. \quad (\text{S35})$$

Assuming that tidal strain amplitude scales with Δg and that dissipated power scales with the square of the strain, the corresponding hemispheric correction factors for the tidally dissipated power are

$$C_{\text{near}} = \left(1 + \frac{3}{2}\varepsilon_R\right)^2, \quad C_{\text{far}} = \left(1 - \frac{3}{2}\varepsilon_R\right)^2, \quad (\text{S36})$$

which both reduce to unity in the point-mass limit $R_{\text{M}}/a_{\text{E-M}} \rightarrow 0$.

At each time step we therefore compute nearside and farside tidal powers simply as

$$\dot{E}_{\text{tide,near}}(t) = C_{\text{near}}(a_{\text{E-M}}(t)) \dot{E}_{\text{tide},0}(a_{\text{E-M}}(t), T_{m,\text{near}}(t)), \quad (\text{S37})$$

$$\dot{E}_{\text{tide,far}}(t) = C_{\text{far}}(a_{\text{E-M}}(t)) \dot{E}_{\text{tide},0}(a_{\text{E-M}}(t), T_{m,\text{far}}(t)), \quad (\text{S38})$$

and evolve two otherwise identical zero-dimensional thermal columns for the nearside and farside using these hemispheric tidal powers. The center-to-center distance $a_{\text{E-M}}(t)$ remains governed by the same Earth-dominated tidal torque as in the symmetric model. The resulting near–far differences in temperature and cliff age are shown in Fig. 4 and Fig. S8.

Supplementary Text

3. Parameter-space exploration

3.1 Sensitivity to initial temperatures

We assess the sensitivity of the tidal heating trajectory to the initial LMO and core temperatures (T_{m0}, T_{c0}) while holding orbital configuration fixed (i.e., $e = 0.05$, $Q_{\text{E}}/k_{2\text{E}} = 400$ for all time) and the initial semi-major axis $a_0 = 3.0 R_{\text{E}}$, matching the example case in the main text. As shown in Fig. S5, different (T_{m0}, T_{c0}) pairs affect only the very early ($\gtrsim 4.499$ Ga) transient period—specifically, the amplitude of the initial \dot{E}_{tide} spike and the precise entry time into the transitional rheology window (where the global melt fraction ≈ 0.7). After this brief start-up, the $\dot{E}_{\text{tide}}(t)$ trajectories rapidly converge and the resulting cliff ages—defined by the solutions of $\dot{E}_{\text{tide}} = \dot{E}_{\text{rad}}$ —are virtually indistinguishable across all tested initial temperatures. Panels B–C of Fig. S5 further show that varying the initial core–mantle temperature offset, ΔT_{c-m} (including $T_{c0} = T_{m0}$ and $T_{c0} = T_{m0} + 50\text{--}100$ K), does not appreciably alter the post-transient evolution or the inferred cliff ages; hence, the model is insensitive to both (T_{m0}, T_{c0}) and ΔT_{c-m} .

3.2 Eccentricity and Earth–Moon distance evolution

Lunar orbital parameters during the LMO epoch are uncertain and lack direct material evidence. As summarized in Eq. (S13), the dominant orbital controls in our tidal calculation are the semi-major axis a and the eccentricity e ; to first order, tidal heating scales as a^{-6} and e^2 . Today, $a \approx 60 R_E$ and $e \approx 0.055$. At earlier times the Moon likely orbited closer to Earth with a larger e , implying stronger tidal dissipation than later in its history. For simplicity, we prescribe a time-varying semi-major axis $a(t)$ and a constant eccentricity over the interval of interest.

Fig. S6 provides a detailed overview of tidal-heating trajectories. Across variations in eccentricity e or the ratio Q_E/k_{2E} , all curves exhibit a robust high plateau-to-sharp cliff pattern. Increasing e or Q_E/k_{2E} (i.e., decreasing the Earth–Moon distance and thus strengthening the effective tidal forcing) sustains higher tidal power for a longer period of time and yields systematically younger cliff ages. Conversely, smaller values lead to an earlier cliff closer to 4.5 Ga.

The evolution of $a(t)$ is governed primarily by tides raised by the Moon on Earth [36]. The recession rate therefore depends on Earth’s tidal response, which we express by the ratio Q_E/k_{2E} and which shows a strong inverse dependence on $a(t)$ (see Eq. (S27)). In the example run of Fig. 1, we adopt $Q_E/k_{2E} = 400$, yielding $a \approx 29.4 R_E$ at 4.35 Ga. This matches previously published reconstructions (see Fig. S4). This choice is also consistent with inclination constraints: strong LMO tidal dissipation would remove orbital inclination. The present lunar inclination of about 5.16° implies that LMO damping could not have persisted while the Moon lingered near $a \approx 20 R_E$, where damping at low obliquity is most efficient [11]. In addition, obliquity can become large near the Cassini-state transition at $a \approx 30 R_E$ [11, 42, 55]; large obliquity greatly enhances obliquity tides, so if the LMO were still dissipative, the inclination would be efficiently damped and a primordial value erased. To avoid such overprinting, the LMO must have largely solidified before the system spent substantial time near that threshold. Accordingly, our adopted $Q_E/k_{2E} = 400$ should be viewed as a practical lower bound that preserves the present inclination under a highly dissipative LMO. It is also worth noting that Earth’s tidal dissipation in the early epoch may have undergone its own transitional rheology, implying strong time variability in Q_E —from low values during highly dissipative states to potentially extremely high values (on the order of 10^{12} – 10^{16}) when dissipation is weak. Pinning down when Earth’s magma ocean solidified, and the corresponding tidal parameters and their impact on the Moon, is important future work but beyond our present scope.

Lunar eccentricity is set by a balance between tidal damping and resonant or secular excitation like evection. Published solutions allow much larger ancient values than our baseline: for synchronous rotation at $a \approx 22.9 R_E$, $e \approx 0.49$ has been inferred, and evection can pump e to ~ 0.5 at $a \approx 4.6 R_E$ [19]. By comparison, we adopt $e = 0.05$, which lies well below these ranges and is therefore very conservative for the interval considered.

Hence, our baseline case adopts a relatively large Earth–Moon distance and a small eccentricity, so the enhanced tidal heating is not driven primarily by orbital forcing but by the LMO’s rheological state.

3.3 Effective volume fraction

Our baseline simulation assumed that the entire LMO participates in the tidal response (effective fraction $f \cdot \phi(T_m)$ with $f = 1$). To test partial participation, we scale tidal dissipation by an

effective participating fraction $f \in (0, 1]$ and, for the baseline orbital configuration (i.e., where $e = 0.05$, $Q_E/k_{2E} = 400$), we reduce f systematically to 0.8, 0.6, 0.4, 0.2, testing the entire evolution each time. The result is a uniformly weaker \dot{E}_{tide} , a shortened high-energy plateau, and systematically older cliff ages (defined by the crossing $\dot{E}_{\text{tide}} = \dot{E}_{\text{rad}}$). However, increasing the eccentricity to $e = 0.10$ —a plausible value for early lunar orbits [18]—compensates for small f , yielding cliff ages near ~ 4.35 Ga or younger. Thus, allowing only a fraction of the LMO to enter the transitional rheology regime still preserves the robust high-plateau–sharp-cliff pattern. Importantly, the $f = 1$ baseline value should not be viewed as an overestimate, given our conservative baseline value for e and the effective forcing ratio Q_E/k_{2E} .

3.4 Age and temperature asymmetry of the LMO

Our model predicts that tidal dissipation differs between the lunar near and farsides and, consequently, that the LMO’s eventual crystallization would potentially develop asymmetries in both temperature and crystallization age (approximately the “cliff age”). We chart these asymmetries across the $(e, Q_E/k_{2E})$ space by quantifying the peak near–far temperature contrast $\max |\Delta T_m|$ and the cliff-age difference $\Delta t_{\text{cliff}} \equiv t_{\text{cliff}}^{\text{near}} - t_{\text{cliff}}^{\text{far}}$ (Fig. S8). For $e \approx 0.10$ and $Q_E/k_{2E} \approx 800$, the model yields a temperature contrast exceeding 85 K and a cliff-age offset of ~ 80 Myr. Our setup remains simplified; future work should incorporate more realistic geometry, rheology, and orbit–thermal coupling.

Table S1: List of the parameters used in the model.

Symbol	Definition	Value
G	Gravitational constant	$6.67430 \times 10^{-11} \text{ m}^3 \text{ kg}^{-1} \text{ s}^{-2}$
σ_B	Stefan–Boltzmann constant	$5.670374419 \times 10^{-8} \text{ W m}^{-2} \text{ K}^{-4}$
R	Universal gas constant	$8.314462618 \text{ J mol}^{-1} \text{ K}^{-1}$
M_E	Earth mass	$5.972 \times 10^{24} \text{ kg}$
R_E	Earth mean radius	$6.371 \times 10^6 \text{ m}$
M_M	Moon mass	$7.342 \times 10^{22} \text{ kg}$
R_M	Lunar mean radius	$1.7371 \times 10^6 \text{ m}$
g	Lunar surface gravity	1.62 m s^{-2}
R_c	Lunar core radius	$3.5 \times 10^5 \text{ m}$
D_m	LMO thickness	$1.3871 \times 10^6 \text{ m}$
ρ	LMO bulk density	3346 kg m^{-3}
c_{LMO}	LMO specific heat capacity	$1200 \text{ J kg}^{-1} \text{ K}^{-1}$
L_{LMO}	Latent heat of fusion	$3.2 \times 10^5 \text{ J kg}^{-1}$
T_s	Solidus temperature	1600 K
T_l	Liquidus temperature	2000 K
T_{cri}	Critical rheological temperature	1760 K
a_c	Nu–Ra prefactor	0.1
Ra_c	Critical Rayleigh number (norm.)	1100
α_T	Thermal expansivity	$3 \times 10^{-5} \text{ K}^{-1}$
k_m	LMO thermal conductivity	$3.75 \text{ W m}^{-1} \text{ K}^{-1}$
κ	Thermal diffusivity	$1.0 \times 10^{-6} \text{ m}^2 \text{ s}^{-1}$
γ	Viscosity-contrast parameter (LBL)	0.011
A	Bond albedo	0.12
L_\star	Stellar luminosity (Sun)	$3.828 \times 10^{26} \text{ W}$
a_\star	Heliocentric distance (1 AU)	$1.496 \times 10^{11} \text{ m}$
ϵ_v	Effective emissivity	0.9
$T_{\text{surf},0}$	Initial surface temperature	250 K
T_{m0}	Initial LMO temperature	3000 K
T_{c0}	Initial core temperature	3100 K
$a_{\text{E–M}}$	Initial Earth–Moon semi-major axis	$3.0 R_E$
e	Orbital eccentricity	0.05
μ_0	Zero-melt reference modulus	$6.5 \times 10^{10} \text{ Pa}$
ϕ_{crit}	Critical melt fraction	0.40
E_a	Activation energy	$3.0 \times 10^5 \text{ J mol}^{-1}$
T_{tot}	Time since lunar formation	4.5 Gyr
$H_{232\text{Th}}$	Specific power (Th-232)	$26.3 \times 10^{-6} \text{ W kg}^{-1}$
$C_{232\text{Th}}$	Bulk conc. (Th-232)	$1.25 \times 10^{-7} \text{ kg kg}^{-1}$
$t_{1/2,232\text{Th}}$	Half-life (Th-232)	14.0 Gyr
$\lambda_{232\text{Th}}$	Decay constant (Th-232)	$1.570 \times 10^{-18} \text{ s}^{-1}$
$H_{238\text{U}}$	Specific power (U-238)	$97.7 \times 10^{-6} \text{ W kg}^{-1}$
$C_{238\text{U}}$	Bulk conc. (U-238)	$3.2759 \times 10^{-8} \text{ kg kg}^{-1}$

List of the parameters used in the model (continued).

Symbol	Definition	Value
$t_{1/2,238\text{U}}$	Half-life (U-238)	4.47 Gyr
$\lambda_{238\text{U}}$	Decay constant (U-238)	$4.917 \times 10^{-18} \text{ s}^{-1}$
$H_{235\text{U}}$	Specific power (U-235)	$574 \times 10^{-6} \text{ W kg}^{-1}$
$C_{235\text{U}}$	Bulk conc. (U-235)	$2.376 \times 10^{-10} \text{ kg kg}^{-1}$
$t_{1/2,235\text{U}}$	Half-life (U-235)	0.704 Gyr
$\lambda_{235\text{U}}$	Decay constant (U-235)	$3.122 \times 10^{-17} \text{ s}^{-1}$
$H_{40\text{K}}$	Specific power (K-40)	$30.4 \times 10^{-6} \text{ W kg}^{-1}$
$C_{40\text{K}}$	Bulk conc. (K-40)	$9.711 \times 10^{-9} \text{ kg kg}^{-1}$
$t_{1/2,40\text{K}}$	Half-life (K-40)	1.25 Gyr
$\lambda_{40\text{K}}$	Decay constant (K-40)	$1.758 \times 10^{-17} \text{ s}^{-1}$
$k_{2,E}$	Earth degree-2 Love number	0.3
Q_E	Earth tidal quality factor	120
M_c	Core mass	$1.6 \times 10^{21} \text{ kg}$
c_c	Core specific heat capacity	$840 \text{ J kg}^{-1} \text{ K}^{-1}$
M_{LMO}	LMO mass ($M_M - M_c$)	$7.182 \times 10^{22} \text{ kg}$
Nu_{max}	Nusselt-number cap (UBL)	10^5
$\eta_{S,\text{sol}}^{\text{ref}}$	Reference shear viscosity at T_{sol}	10^{19} Pa s
$\eta_{S,\text{cri}}^{\text{ref}}$	Reference shear viscosity at T_{cri}	$3.5 \times 10^{12} \text{ Pa s}$
$\eta_{S,\text{liq}}^{\text{ref}}$	Reference shear viscosity at T_{liq}	10^{-3} Pa s
A_ϕ	Melt-weakening coefficient in viscosity law	40
η_{min}	Minimum allowed viscosity	10^{-6} Pa s
η_{max}	Maximum allowed viscosity	10^{27} Pa s

Earth's gravitational forcing

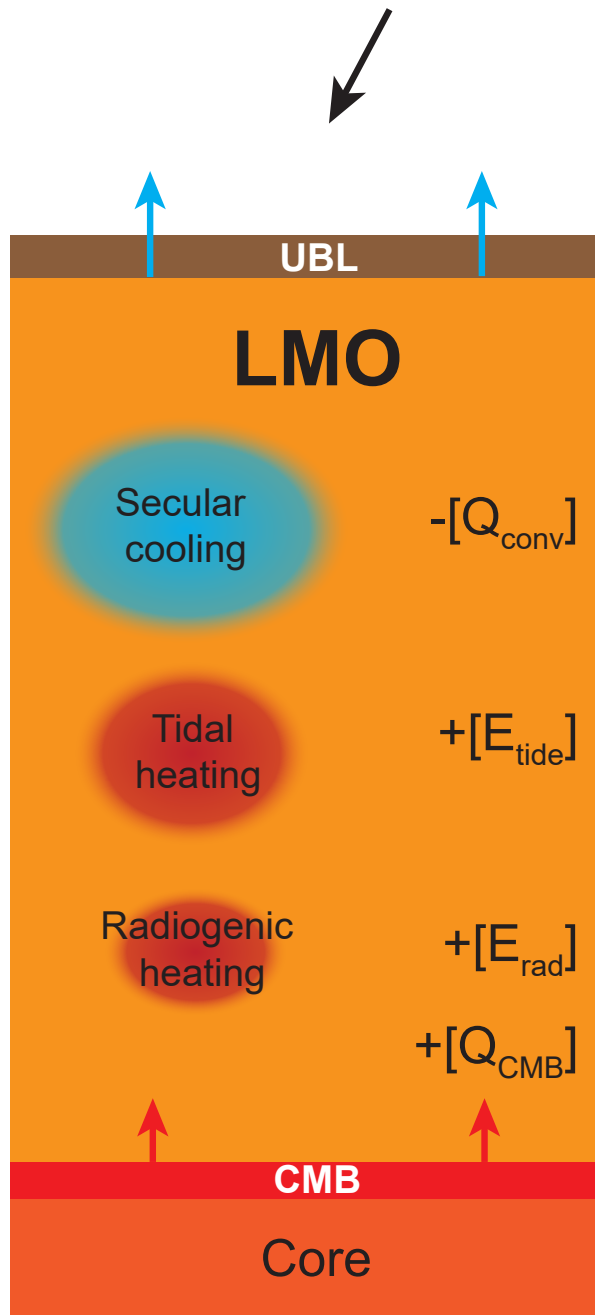


Figure S1: Schematic diagram illustrating the thermal energy budget of the LMO.

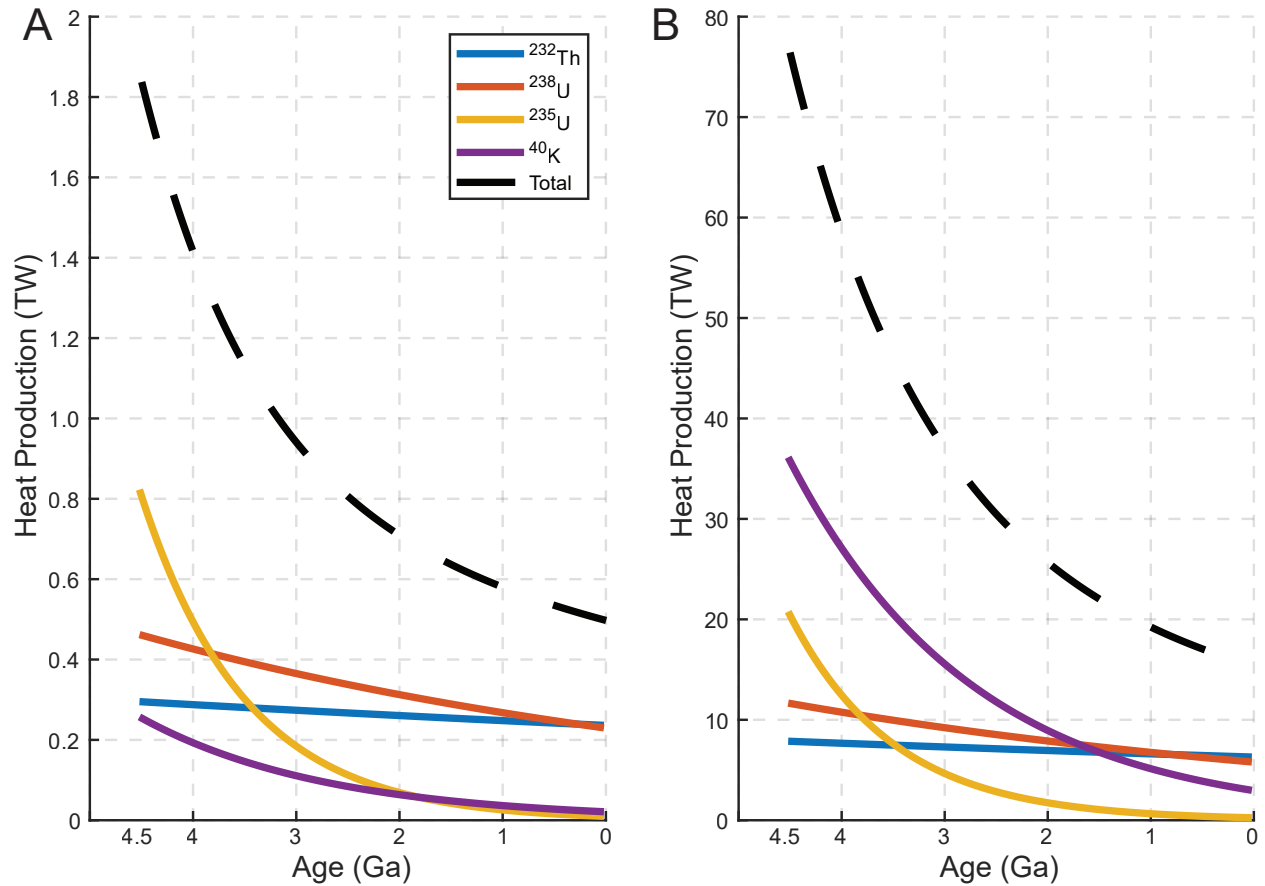


Figure S2: **Radiogenic heat production rate of the Moon and the Earth.** Time evolution of radiogenic heat production in the mantles of the Moon and the Earth, based on decay of four key heat-producing isotopes: ^{232}Th , ^{238}U , ^{235}U , and ^{40}K . Colored solid lines represent the contribution of each isotope, and the thick black dashed line denotes the total radiogenic heat production. (A) Radiogenic heat in the lunar mantle decreases from an initial value of approximately 1.9 TW at 4.5 Ga to less than 0.5 TW at present, with ^{238}U and ^{232}Th dominating at later times. (B) Radiogenic heat in the Earth's mantle starts at ~ 75 TW and declines to ~ 20 TW today, with ^{40}K as the dominant early contributor. The stronger and more sustained radiogenic power in Earth compared to the Moon highlights the latter's limited internal heat budget. The data of elemental concentration are from [4, 53].

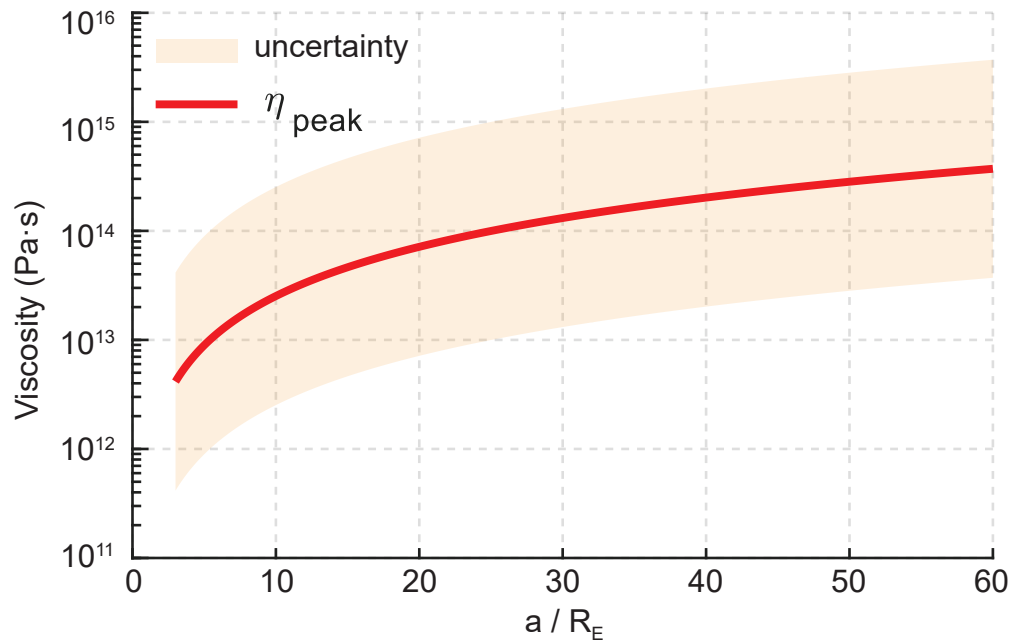


Figure S3: **Peak tidal viscosity vs. Earth–Moon distance.** The red curve shows the peak viscosity $\eta_{\text{peak}}(a)$ from Eq. (S26), which corresponds to tidal-heating maximum. The shaded region illustrates an uncertainty band equal to a factor of ten around η_{peak} —i.e., $[\eta_{\text{peak}}/10, 10 \eta_{\text{peak}}]$ —to account for uncertainties in rheology and forcing frequency. Material parameters are listed in Table S1. Over $a = 3\text{--}60 R_E$, η_{peak} lies within the transitional-rheology window ($\sim 10^{12}\text{--}10^{16}$ Pa s).

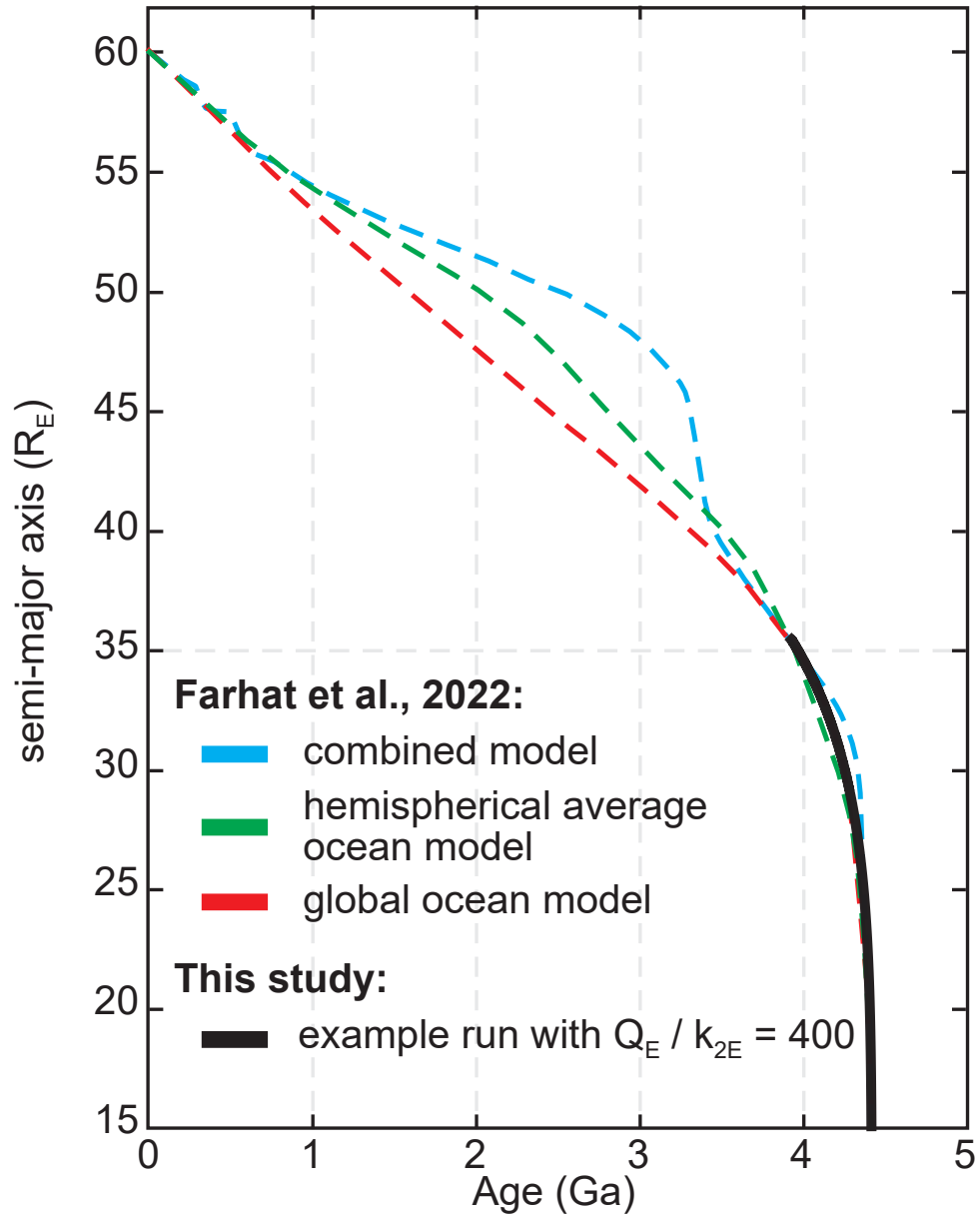


Figure S4: Semi-major axis evolution from 4.5 to 4.0 Ga of this work compared to Farhat et al. (2022) [18].

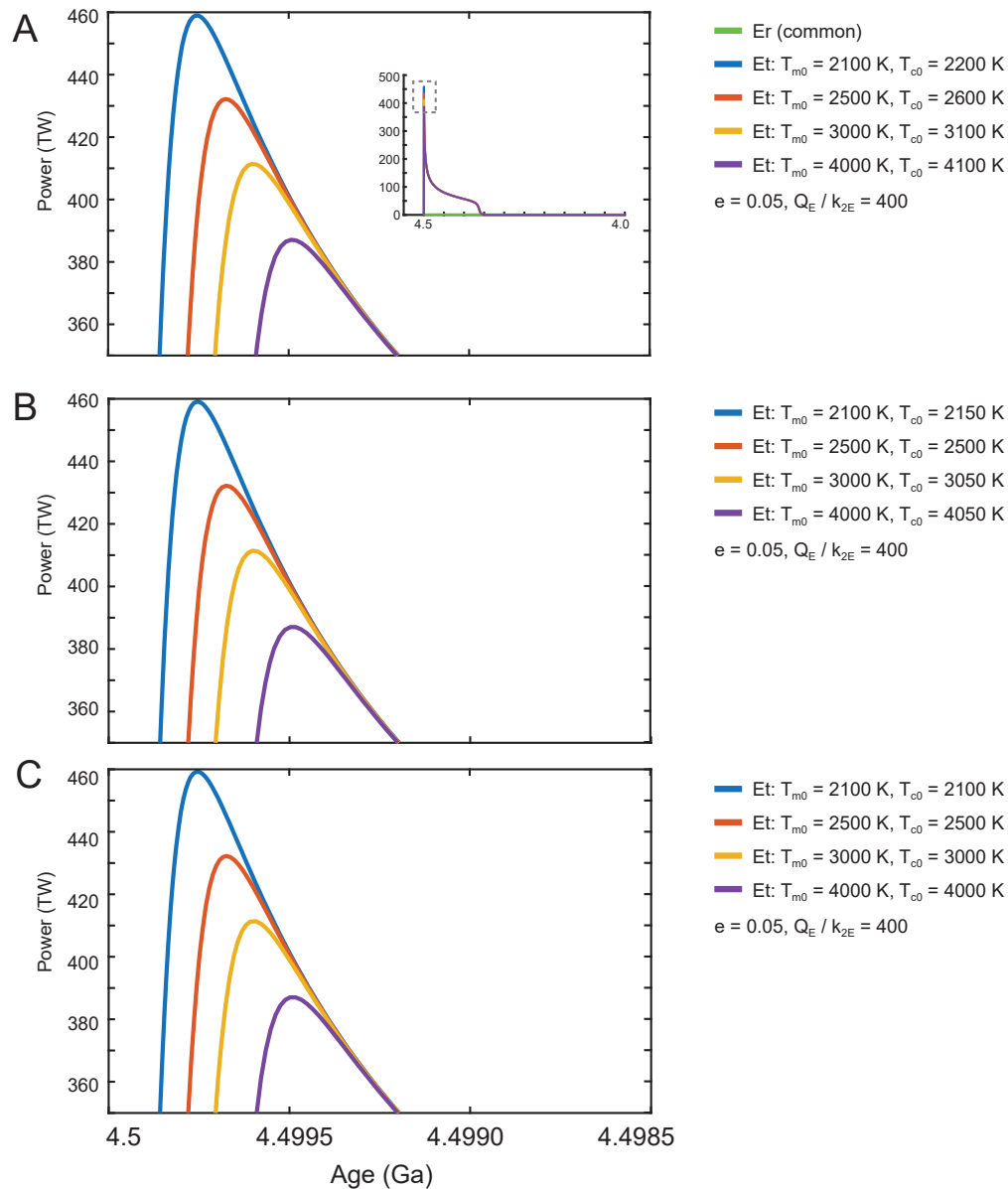


Figure S5: Initial LMO and core temperature sensitivity of tidal heating. Tidal dissipation power E_t (colored curves) compared across four initial LMO/core temperature pairs (T_{m0} , T_{c0}) while holding orbital forcing fixed ($e = 0.05$, $Q_E/k_{2E} = 400$). The common green line is radiogenic heating E_r (same in all cases). Higher (T_{m0} , T_{c0}) shift only the short early-time transient—i.e., the entry timing into the transitional-rheology window—and slightly the peak E_t . After the brief start-up, trajectories rapidly converge and the subsequent plateau and the crossing with E_r (“cliff” onset) occur at practically the same age and power across all initial-temperature choices. The inset shows the full early spike and the rapid relaxation onto a common track. Panels A–C use different initial core–mantle offsets, but the conclusion is unchanged.

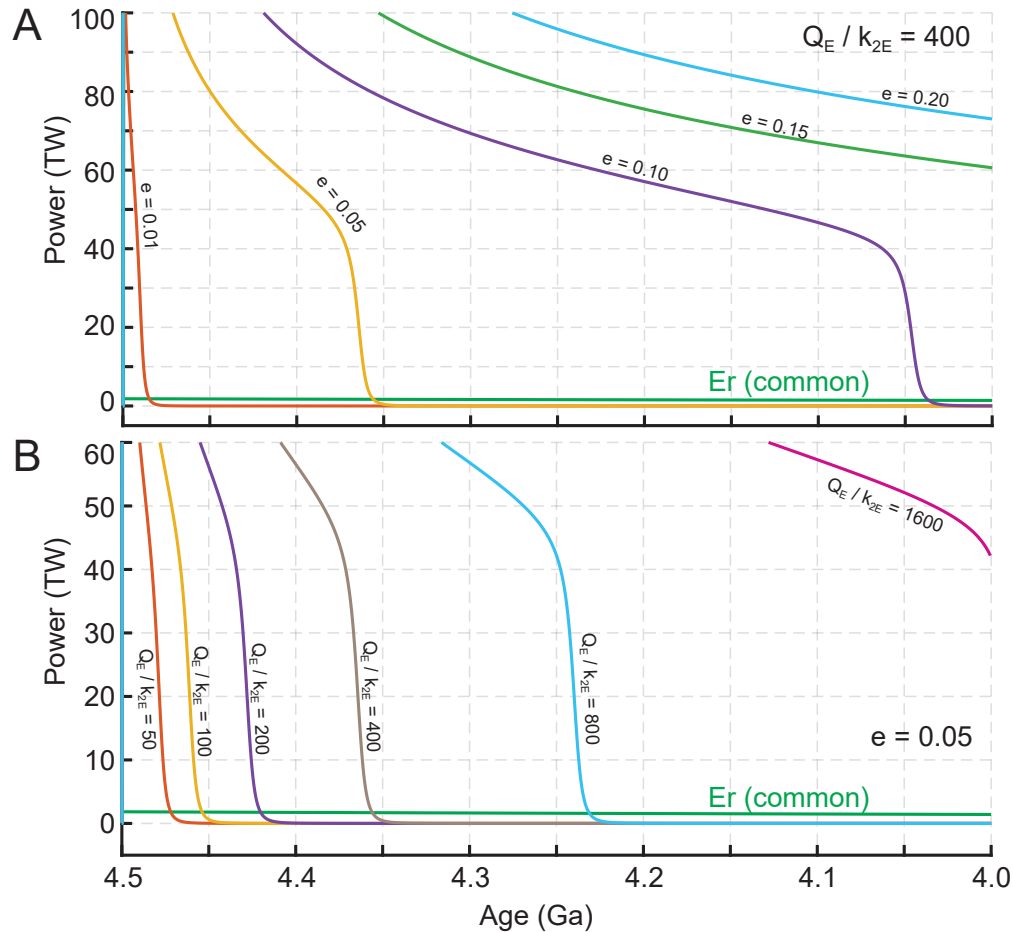


Figure S6: **Tidal-heating evolution and cliff ages across eccentricities and Earth–Moon distances.** (A) Tidal-heating power \dot{E}_{tide} for several eccentricities e at fixed orbital forcing ratio $Q_E/k_{2E} = 400$. (B) \dot{E}_{tide} for several Q_E/k_{2E} at fixed $e = 0.05$. In both panels, the green line is the common radiogenic heating \dot{E}_{rad} . Larger e or larger Q_E/k_{2E} sustain higher tidal power for longer, delaying the cliff, whereas small e or small Q_E/k_{2E} produce an early cliff shortly after 4.5 Ga. Labels on curves mark parameter values. Note: varying Q_E/k_{2E} changes the $a(t)$ history (through Eq. (S27)); the curves are shown at their self-consistent $a(t)$.

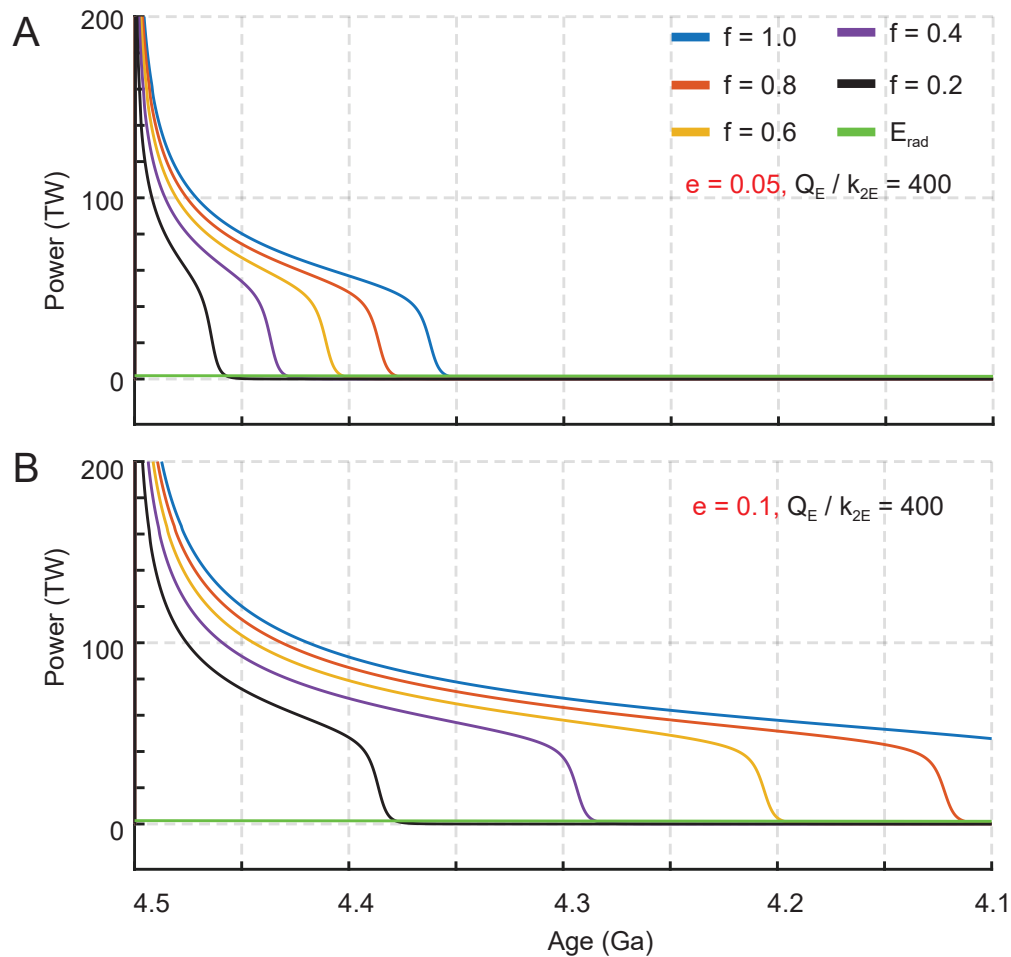


Figure S7: **Effect of a volumetric participation factor on tidal heating.** Colored curves show \dot{E}_{tide} computed with a multiplicative volume coefficient $f \in \{1.0, 0.8, 0.6, 0.4, 0.2\}$ applied during integration; the green line is the common radiogenic heating \dot{E}_{rad} . **(A)** $e = 0.05$ and $Q_E/k_{2E} = 400$. **(B)** $e = 0.10$ and $Q_E/k_{2E} = 400$. Decreasing f uniformly lowers the tidal power and advances the cliff age—defined by the crossing $\dot{E}_{\text{tide}} = \dot{E}_{\text{rad}}$ —whereas larger f sustains higher power for longer and delays the cliff. At higher eccentricity **(B)**, stronger forcing reduces the sensitivity to f and shifts the cliff to younger ages overall. Legends/labels indicate the adopted f values.

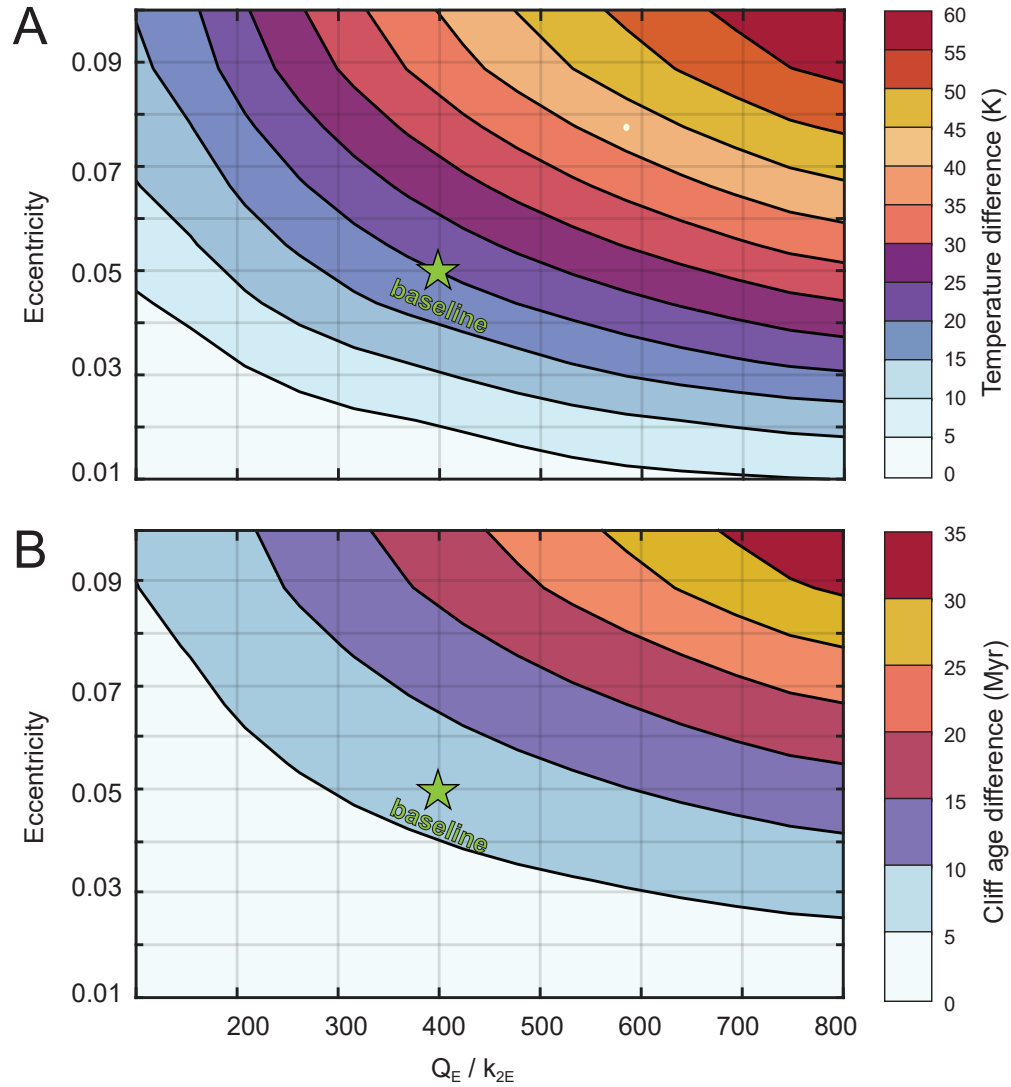


Figure S8: **Near-far side asymmetries across the $(e, Q_E/k_{2E})$ space.** (A) Peak near-far mantle temperature contrast, $\max |\Delta T_m|$ (K). (B) Cliff-age difference, $\Delta t_{\text{cliff}} \equiv t_{\text{cliff}}^{\text{near}} - t_{\text{cliff}}^{\text{far}}$ (Myr); positive values mean the far side reaches the cliff earlier than the near side. Our example runs are indicated by green pentagons.

References

- [1] Yutaka Abe. Thermal and chemical evolution of the terrestrial magma ocean. *Physics of the Earth and Planetary Interiors*, 100(1-4):27–39, 1997.
- [2] Jeffrey C Andrews-Hanna, Renee C Weber, Ian Garrick-Bethell, Alexander J Evans, Walter S Kiefer, Robert E Grimm, James T Keane, Matthieu Laneuville, Yoshiaki Ishihara, Shunichi Kamata, et al. The structure and evolution of the lunar interior. *Reviews in Mineralogy and Geochemistry*, 89(1):243–292, 2023.
- [3] Tomoko Arai, Hiroshi Takeda, Akira Yamaguchi, and Makiko Ohtake. A new model of lunar crust: asymmetry in crustal composition and evolution. *Earth, Planets and Space*, 60(4): 433–444, 2008.
- [4] Ricardo Arevalo Jr, William F McDonough, and Mario Luong. The k/u ratio of the silicate earth: Insights into mantle composition, structure and thermal evolution. *Earth and Planetary Science Letters*, 278(3-4):361–369, 2009.
- [5] Avner A Arzi. Critical phenomena in the rheology of partially melted rocks. *Tectonophysics*, 44(1-4):173–184, 1978.
- [6] Melanie Barboni, Patrick Boehnke, Brenhin Keller, Issaku E Kohl, Blair Schoene, Edward D Young, and Kevin D McKeegan. Early formation of the moon 4.51 billion years ago. *Science advances*, 3(1):e1602365, 2017.
- [7] Carver J Bierson. The impact of rheology model choices on tidal heating studies. *Icarus*, 414:116026, 2024.
- [8] Lars E Borg and Richard W Carlson. The evolving chronology of moon formation. *Annual Review of Earth and Planetary Sciences*, 51(1):25–52, 2023.
- [9] Lars E Borg, James N Connelly, Maud Boyet, and Richard W Carlson. Chronological evidence that the moon is either young or did not have a global magma ocean. *Nature*, 477(7362): 70–72, 2011.
- [10] Lars E Borg, Amy M Gaffney, and Charles K Shearer. A review of lunar chronology revealing a preponderance of 4.34–4.37 ga ages. *Meteoritics & Planetary Science*, 50(4):715–732, 2015.
- [11] Erinna MA Chen and Francis Nimmo. Tidal dissipation in the lunar magma ocean and its effect on the early evolution of the earth–moon system. *Icarus*, 275:132–142, 2016.
- [12] Zexian Cui, Qing Yang, Yan-Qiang Zhang, Chengyuan Wang, Haiyang Xian, Zhiming Chen, Zhiyong Xiao, Yuqi Qian, James W Head III, Clive R Neal, et al. A sample of the moon’s far side retrieved by chang’e-6 contains 2.83-billion-year-old basalt. *Science*, 386(6728): 1395–1399, 2024.
- [13] Matija Čuk, Simon J Lock, Sarah T Stewart, and Douglas P Hamilton. Tidal evolution of the earth–moon system with a high initial obliquity. *The Planetary Science Journal*, 2(4):147, 2021.

- [14] Michael Efroimsky. Bodily tides near spin–orbit resonances. *Celestial Mechanics and Dynamical Astronomy*, 112(3):283–330, 2012.
- [15] Michael Efroimsky. Tidal dissipation compared to seismic dissipation: In small bodies, earths, and super-earths. *The Astrophysical Journal*, 746(2):150, 2012.
- [16] Linda T Elkins-Tanton. Magma oceans in the inner solar system. *Annual Review of Earth and Planetary Sciences*, 40(1):113–139, 2012.
- [17] Linda T Elkins-Tanton, Seth Burgess, and Qing-Zhu Yin. The lunar magma ocean: Reconciling the solidification process with lunar petrology and geochronology. *Earth and Planetary Science Letters*, 304(3-4):326–336, 2011.
- [18] Mohammad Farhat, Pierre Auclair-Desrotour, Gwenaël Boué, and Jacques Laskar. The resonant tidal evolution of the earth-moon distance. *Astronomy & Astrophysics*, 665:L1, 2022.
- [19] Ian Garrick-Bethell, Jack Wisdom, and Maria T Zuber. Evidence for a past high-eccentricity lunar orbit. *Science*, 313(5787):652–655, 2006.
- [20] Juliane Gross, Allan H Treiman, and Celestine N Mercer. Lunar feldspathic meteorites: Constraints on the geology of the lunar highlands, and the origin of the lunar crust. *Earth and Planetary Science Letters*, 388:318–328, 2014.
- [21] Yuji Harada, Sander Goossens, Koji Matsumoto, Jianguo Yan, Jinsong Ping, Hiroto Noda, and Junichi Haruyama. Strong tidal heating in an ultralow-viscosity zone at the core–mantle boundary of the moon. *Nature Geoscience*, 7(8):569–572, 2014.
- [22] Huicun He, Linxi Li, Sen Hu, Yubing Gao, Liang Gao, Zhan Zhou, Mengfan Qiu, Disheng Zhou, Huanxin Liu, Ruiying Li, et al. Water abundance in the lunar farside mantle. *Nature*, pages 1–5, 2025.
- [23] Sheng He, Yang Li, Xuelin Zhu, Jian Chen, Ziyang Li, Ting Li, Jun Zhong, Jing Tan, Qian He, Zhuoyue Fu, et al. A relatively cool lunar farside mantle inferred from chang’e-6 basalts and remote sensing. *Nature Geoscience*, pages 1–6, 2025.
- [24] Wade G Henning, Richard J O’Connell, and Dimitar D Sasselov. Tidally heated terrestrial exoplanets: viscoelastic response models. *The Astrophysical Journal*, 707(2):1000, 2009.
- [25] WG Henning, JP Renaud, M Efroimsky, TA Hurford, and S Goossens. Increased lunar tidal heating due to consideration of higher order terms in eccentricity and advanced rheological modeling. In *55th Lunar and Planetary Science Conference*, volume 3040, page 1316, 2024.
- [26] Debra M Hurwitz and David A Kring. Differentiation of the south pole–aitken basin impact melt sheet: Implications for lunar exploration. *Journal of Geophysical Research: Planets*, 119(6):1110–1133, 2014.
- [27] William M Kaula. Tidal dissipation by solid friction and the resulting orbital evolution. *Reviews of geophysics*, 2(4):661–685, 1964.

- [28] Zdeněk Kopal. Gravitational heating of the moon. *Icarus*, 1(1-6):412–421, 1962.
- [29] Jun Korenaga. Rapid solidification of earth’s magma ocean limits early lunar recession. *Icarus*, 400:115564, 2023.
- [30] Jun Korenaga. Tidal dissipation within earth’s solidifying magma ocean: Iii. effects of matrix compaction. *Icarus*, page 116759, 2025.
- [31] Jun Korenaga. Tidal dissipation within earth’s solidifying magma ocean: I. effects of inertia and lunar orbital eccentricity. *Icarus*, page 116756, 2025.
- [32] Jun Korenaga. Tidal dissipation within earth’s solidifying magma ocean: Ii. atmospheric blanketing and its constraint on tidal heating. *Icarus*, page 116743, 2025.
- [33] Thomas Lebrun, H el ene Massol, Eric Chassefi ere, Anne Davaille, Emmanuel Marcq, Philippe Sarda, Fran ois Leblanc, and Genevi eve Brandeis. Thermal evolution of an early magma ocean in interaction with the atmosphere. *Journal of Geophysical Research: Planets*, 118(6): 1155–1176, 2013.
- [34] Zhuangzhuang Liu, Lieven Pandelaers, Bart Blanpain, and Muxing Guo. Viscosity of heterogeneous silicate melts: assessment of the measured data and modeling. *ISIJ International*, 57(11):1895–1901, 2017.
- [35] Valeri V Makarov and Michael Efroimsky. Tidal dissipation in a homogeneous spherical body. ii. three examples: Mercury, io, and kepler-10 b. *The Astrophysical Journal*, 795(1):7, 2014.
- [36] Carl D Murray and Stanley F Dermott. *Solar system dynamics*. Cambridge university press, 1999.
- [37] Harrison Nicholls, Claire Marie Guimond, Hamish CFC Hay, Richard D Chatterjee, Tim Lichtenberg, and Raymond T Pierrehumbert. Self-limited tidal heating and prolonged magma oceans in the 1 98-59 system. *Monthly Notices of the Royal Astronomical Society*, 541(3): 2566–2584, 2025.
- [38] F Nimmo and DJ Stevenson. Influence of early plate tectonics on the thermal evolution and magnetic field of mars. *Journal of Geophysical Research: Planets*, 105(E5):11969–11979, 2000.
- [39] Francis Nimmo, Thorsten Kleine, and Alessandro Morbidelli. Tidally driven remelting around 4.35 billion years ago indicates the moon is old. *Nature*, 636(8043):598–602, 2024.
- [40] Makiko Ohtake, Hiroshi Takeda, Tsuneo Matsunaga, Yasuhiro Yokota, Junichi Haruyama, Tomokatsu Morota, Satoru Yamamoto, Yoshiko Ogawa, Takahiro Hiroi, Yuzuru Karouji, et al. Asymmetric crustal growth on the moon indicated by primitive farside highland materials. *Nature Geoscience*, 5(6):384–388, 2012.
- [41] RS Park, A Berne, AS Konopliv, JT Keane, I Matsuyama, Francis Nimmo, M Rovira-Navarro, MP Panning, M Simons, DJ Stevenson, et al. Thermal asymmetry in the moon’s mantle inferred from monthly tidal response. *Nature*, pages 1–5, 2025.

- [42] Stanton J Peale. Generalized cassini's laws. *Astronomical Journal*, Vol. 74, p. 483 (1969), 74:483, 1969.
- [43] Stanton J Peale and Patrick Cassen. Contribution of tidal dissipation to lunar thermal history. *Icarus*, 36(2):245–269, 1978.
- [44] Alice C Quillen, Larkin Martini, and Miki Nakajima. Near/far side asymmetry in the tidally heated moon. *Icarus*, 329:182–196, 2019.
- [45] Joe P Renaud and Wade G Henning. Increased tidal dissipation using advanced rheological models: Implications for io and tidally active exoplanets. *The Astrophysical Journal*, 857(2): 98, 2018.
- [46] Sandeep Sahijpal and Vishal Goyal. Thermal evolution of the early moon. *Meteoritics & Planetary Science*, 53(10):2193–2211, 2018.
- [47] Max W Schmidt and Giuliano Kraetli. Experimental crystallization of the lunar magma ocean, initial selenotherm and density stratification, and implications for crust formation, overturn and the bulk silicate moon composition. *Journal of Geophysical Research: Planets*, 127(5):e2022JE007187, 2022.
- [48] M Segatz, T Spohn, MN Ross, and G Schubert. Tidal dissipation, surface heat flow, and figure of viscoelastic models of io. *Icarus*, 75(2):187–206, 1988.
- [49] Daigo Shoji and Kei Kurita. Thermal–orbital coupled tidal heating and habitability of martian-sized extrasolar planets around m stars. *The Astrophysical Journal*, 789(1):3, 2014.
- [50] V Solomatov. Magma oceans and primordial mantle differentiation. In *Evolution of the Earth*, pages 81–104. Elsevier Inc., 2015.
- [51] Bin Su, Yi Chen, Zeling Wang, Di Zhang, Haojie Chen, Sheng Gou, Zongyu Yue, Yanhong Liu, Jiangyan Yuan, Guoqiang Tang, et al. South pole–aitken massive impact 4.25 billion years ago revealed by chang'e-6 samples. *National Science Review*, 12(6):nwaf103, 2025.
- [52] Hiroshi Takeda, A Yamaguchi, DD Bogard, Y Karouji, M Ebihara, M Ohtake, K Saiki, and T Arai. Magnesian anorthosites and a deep crustal rock from the farside crust of the moon. *Earth and Planetary Science Letters*, 247(3-4):171–184, 2006.
- [53] Stuart Ross Taylor. Lunar and terrestrial crusts: a contrast in origin and evolution. *Physics of the Earth and Planetary Interiors*, 29(3-4):233–241, 1982.
- [54] Robert H Tyler, Wade G Henning, and Christopher W Hamilton. Tidal heating in a magma ocean within jupiter's moon io. *The Astrophysical Journal Supplement Series*, 218(2):22, 2015.
- [55] William Roger Ward. Tidal friction and generalized cassini's laws in the solar system. *Astronomical Journal*, vol. 80, Jan. 1975, p. 64-70., 80:64–70, 1975.

- [56] Paul H Warren. The magma ocean concept and lunar evolution. *IN: Annual review of earth and planetary sciences. Volume 13. Palo Alto, CA, Annual Reviews, Inc., 1985, p. 201-240., 13:201–240, 1985.*
- [57] John T Wasson and Paul H Warren. Contribution of the mantle to the lunar asymmetry. *Icarus*, 44(3):752–771, 1980.
- [58] Mark A Wieczorek, Gregory A Neumann, Francis Nimmo, Walter S Kiefer, G Jeffrey Taylor, H Jay Melosh, Roger J Phillips, Sean C Solomon, Jeffrey C Andrews-Hanna, Sami W Asmar, et al. The crust of the moon as seen by grail. *Science*, 339(6120):671–675, 2013.
- [59] Kevin J Zahnle, Roxana Lupu, Anthony Dobrovolskis, and Norman H Sleep. The tethered moon. *Earth and Planetary Science Letters*, 427:74–82, 2015.
- [60] Huijuan Zhang, Wei Yang, Di Zhang, Jialong Hao, Xiaoying Liu, Honggang Zhu, Ross N Mitchell, Lihui Jia, Yunhong Fan, Shitou Wu, et al. A more reduced mantle beneath the lunar south pole–aitken basin. *Nature Communications*, 16(1):6985, 2025.
- [61] Qian WL Zhang, Mu-Han Yang, Qiu-Li Li, Yu Liu, Zong-Yu Yue, Qin Zhou, Liu-Yang Chen, Hong-Xia Ma, Sai-Hong Yang, Xu Tang, et al. Lunar farside volcanism 2.8 billion years ago from chang’e-6 basalts. *Nature*, 643(8071):356–360, 2025.
- [62] Wenbo Zhang and Nan Zhang. Long-lived lunar mare volcanism powered by radiogenic and tidal heating. *Journal of Geophysical Research: Planets*, 130(10):e2024JE008828, 2025.
- [63] Qin Zhou, Wei Yang, Zhuyin Chu, Honggang Zhu, Saihong Yang, Xingguo Zeng, Ding-Shuai Xue, Li-Hui Jia, Guangliang Zhang, Hongbo Zhang, et al. Ultra-depleted mantle source of basalts from the south pole–aitken basin. *Nature*, 643(8071):371–375, 2025.